Acceleration-based classification and evolution of fluid flow structures in two-dimensional turbulence

Tristan Faber* and J. C. Vassilicos†

Department of Aeronautics and Institute for Mathematical Sciences, Imperial College, London SW7 2AZ, United Kingdom
(Received 21 August 2009; revised manuscript received 21 March 2010; published 23 August 2010)

Zero acceleration points (ZAPs) and flow structures around them are studied in a direct numerical simulation of two-dimensional energy-cascading stationary homogeneous isotropic turbulence with an extended $k^{-5/3}$ energy spectrum. A well-defined classification of ZAPs in terms of the acceleration gradient tensor's ($\nabla \mathbf{a}$) invariants emerges naturally as a result of well-defined properties of and relations between these invariants at ZAPs. About half of all ZAPs are anti-ZAPs [with $\det(\nabla \mathbf{a}) < 0$] and the number of vortical and straining ZAPs [with $\det(\nabla \mathbf{a}) > 0$] is about the same. Vortical and straining ZAPs are swept by the local fluid velocity to a good statistical approximation whereas anti-ZAPs, which are present in every vortical and straining ZAP's creation and destruction events, are not. The average lifetime of ZAPs seems to scale with the time scale of the smallest eddies in the turbulence, though ZAPs (in particular vortical ones) are able to survive up to a few integral time scales. Our ZAP classification can also be applied to extended flow regions and it turns out that vortical and straining regions are mediated by regions containing anti-ZAPs. A discussion of the length scales and sizes characterizing these regions and the distances between ZAPs is also given.

I. INTRODUCTION

Since the discovery of both large-scale and small-scale coherent structures in two-dimensional and three-dimensional turbulence and the realization of their central importance in understanding turbulent flow properties [1–7], much work has been devoted to characterizing and classifying such structures. Much of this classification work has concentrated on velocity gradient and pressure properties [8,9] because of the natural expectation that vorticity dynamics underpins the evolution of suitably defined coherent structures.

Perhaps the first and most accessible goal in the general study of how coherent structures might explain and help model turbulence properties concerns turbulent mixing properties [10,11]. The application to mixing has motivated the introduction of Lagrangian coherent structures [12] and of a space-filling type of structures called *dissipation elements* [13]. A particular aspect of turbulent mixing, namely, Richardson pair diffusion, has recently been explained in terms of statistics of stagnation points [14–17]. These are critical points of the instantaneous velocity field which Perry and his coworkers [18–20] first used for their dynamical systems classification of turbulent flow regions. More recent works have uncovered the multiscale spatial skeleton of velocity stagnation points in the bulk of the turbulence [[15,16,21], and references therein] and have also related them to *zero-acceleration points* (ZAPs) which define their persistence and that of streamlines during the evolution of the flow [22]. Points where the fluid acceleration is zero (ZAPs) have also turned out to be crucial in explaining the phenomenon of preferential concentration (clustering) of heavy yet small inertial particles in a turbulent carrier fluid, e.g. water droplets in air as in clouds [23–26].

To our knowledge, a first attempt at a classification of different turbulent flow regions in terms of a criterion based on the acceleration gradient tensor was made by Hua and Klein in 1998 [27] who compared it to the Okubo-Weiss criterion [9,28]. These authors introduced a criterion based on the eigenvalues of the acceleration gradient tensor instead of the velocity gradient tensor so as to relate turbulent stirring to the local topography of the flow in a way that can take some account of the unsteadiness in the equations of motion.

All in all, a flow-region classification based on and derived from zero-acceleration points promises to have an impact on turbulent mixing of passive contaminants and turbulent clustering of inertial particles; and use of the acceleration gradient tensor for such a classification is likely to take some account of the unsteadiness of the flow, an issue central to the very concept of coherent structure which alludes as much to the particular shape of the local flow pattern as to the persistence of this shape's identity during dynamic flow evolution.

The first attempt at classifying ZAPs, which was in fact incomplete, was made by Goto and Vassilicos (2004) [16]. They used the divergence of the acceleration gradient tensor which is equivalent to the Okubo-Weiss criterion. In this paper we propose a classification of the vast majority of ZAPs in two-dimensional energy cascading turbulence in terms of a full description of the acceleration gradient tensor. This description and classification also allows us to characterize the persistence and lifetime of ZAPs, including their related creation, sweeping, and destruction properties. Finally, it allows us to introduce a new classification of extended flow regions (ZAPs and their surroundings) which incorporates some understanding of the size of these regions, the inner flow structure of some of these regions and the way they fit together in two-dimensional (2D) space.

This paper is organized as follows: After reminding the reader of some basic ZAP properties, we document the nu-

*t.faber06@imperial.ac.uk
†j.c.vassilicos@imperial.ac.uk

merical methods used in this work and we then introduce our proposed classification. The remainder of the paper discusses sweeping and lifetime properties of the various ZAP classes and finally explores the local neighborhood of certain ZAP types.

II. ZAP BASICS: VELOCITY, CREATION AND DESTRUCTION

A. Definition of ZAPs and their velocity

A *zero-acceleration point*, $\mathbf{x_a}$, is defined as a point where the fluid acceleration vector vanishes,

$$\mathbf{a}(\mathbf{x_a}, t) = 0. \tag{1}$$

The velocity of this ZAP, $\mathbf{V_a}(t)$, is then defined by [24]

$$\frac{\partial \mathbf{a}(\mathbf{x_a}, t)}{\partial t} + \mathbf{V_a}(t) \cdot \nabla \mathbf{a}(\mathbf{x_a}, t) = 0. \tag{2}$$

Clearly, the ZAP velocity $\mathbf{V_a}$, and therefore the motion of the ZAP, depends on the acceleration gradient tensor.

B. Creation and destruction of ZAPs

A ZAP is a topological object of the acceleration field, not a physical one like a fluid element. In a turbulent flow, which is not static but inherently fluctuating, the topologies of the velocity and acceleration fields can and do change with time. Thus, ZAPs in such flows do not exist forever, but are created and destroyed in the course of a flow's evolution.

The creation and destruction events take place when a ZAP trajectory intersects a region where the determinant of the acceleration gradient tensor vanishes, $\det(\nabla \mathbf{a}) = 0$, as in such a case it is generally not possible to invert Eq. (2) and obtain a finite $\mathbf{V_a}$,

$$\mathbf{V_a} = -\frac{1}{\det(\nabla \mathbf{a})} \begin{bmatrix} \det(\partial_t \mathbf{a}, \partial_y \mathbf{a}) \\ \det(\partial_x \mathbf{a}, \partial_t \mathbf{a}) \end{bmatrix}. \tag{3}$$

Whenever $\det(\nabla \mathbf{a}) \neq 0$, $\mathbf{V_a}$ is well defined and the ZAP will still exist an infinitesimal time later (and have existed an infinitesimal time earlier).

In a dynamical systems context, ZAPs would be critical points of the acceleration vector field. It is well known that such critical points in an unsteady two dimensional vector field are created and destroyed in pairs. These events are called *saddle-node* or *fold bifurcations* [29,30] and occur when the determinant of the vector field's Jacobian matrix vanishes, e.g. for the purpose of this paper, when $\det(\nabla \mathbf{a}) = 0$ for ZAPs. They always involve one critical point with a negative determinant of the Jacobian and one critical point with a positive determinant. A classification of ZAPs which complements that of Goto and Vassilicos [16] by taking into account both $\nabla \cdot \mathbf{a}$ and $\det(\nabla \mathbf{a})$ (instead of $\nabla \cdot \mathbf{a}$ only) will be able to account for creation and destruction events. If the Jacobian's eigenvalues do not have an imaginary part, bifurcations of this kind are the only possibility for critical points to be created and destroyed. These observations come into their own in Secs. IV–VI.
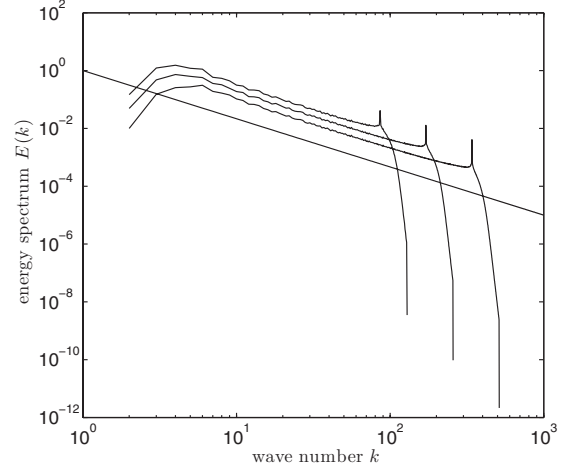

FIG. 1. Energy spectra of all three unfiltered runs A2, B3, and C4, top to bottom. The solid line is $\propto k^{-5/3}$. The sharp peak close to the highest wave numbers of each run is due to the forcing. Note the sharp fall-off of the spectrum at these highest wave numbers which is due to the eighth order hyper viscosity. The energy spectrum at the highest wave number is several orders of magnitude smaller that the energy in the inertial range, and hence, the resolution of the DNS is deemed sufficient to resolve even the smallest features in the flow.

III. NUMERICAL METHODS

The flow investigated in this paper is a two-dimensional stationary homogeneous isotropic turbulent flow in a periodic box of length 2π with an inverse energy cascade giving rise to an energy spectrum $\propto k^{-5/3}$, as shown in Fig. 1. All data in this paper were obtained from different runs of the direct numerical simulation (DNS) scheme described in [16] with the parameters defined and given in Table I. The DNS scheme integrates in time (t) the modified vorticity (ω) equation,

$$\frac{\partial \omega}{\partial t} = \nabla \times [\mathbf{u} \times \omega] + \hat{D}\omega + \mathbf{f}, \tag{4}$$

using a fourth order Runge-Kutta scheme in wave number ($\mathbf{k}$-) space, with the nonlinear term being calculated in real space. The fluid velocity is denoted $\mathbf{u}$ and $\mathbf{f}$ is the forcing. The dissipation operator $\hat{D}$ is defined as

$$\hat{D} = [-\nu\Delta^8 + \alpha\Delta^{-1}], \tag{5}$$

and allows the dissipation of large scales in two-dimensional flows through hyperdrag (α term) as well as narrows the enstrophy cascade in spectral space by using an eighth order Laplacian dissipation term. The resolutions employed for the different runs are listed in Table I.

The acceleration $\mathbf{a}$ and its spatial derivatives, $\nabla \mathbf{a}$, are calculated from the vorticity using spectral derivatives and the right hand side of the modified Navier-Stokes without forcing,

TABLE I. Parameters used in the numerical scheme as described in [16]: the number of grid points[a] N^2, forcing wave number k_f, ratio of forcing wave number range β, magnitude of fixed Fourier component of vorticity $\widetilde{\omega}_0$, time increment of temporal integration dt, and hyperviscosity coefficient ν. The hyperdrag coefficient α is identical for all runs: $\alpha=2.5$. "n" in An, Bn, and Cn enumerates the different cutoff wave numbers employed in the different runs as detailed in Table II.

Run	N^2	k_f	β	$\widetilde{\omega}_0$	dt	ν
An	256^2	85	1.0118	1.05	4.9×10^{-4}	5.00×10^{-31}
Bn	512^2	170	1.0059	0.83	2.5×10^{-4}	1.54×10^{-35}
Cn	1024^2	340	1.0029	0.66	1.2×10^{-4}	4.90×10^{-40}

[a]The definition of N in this paper differs from the original use in [16], which we shall denote N^*. Here it is the number of grid points for the vorticity field, whereas in [16] it is the number of grid points in the dealiased scheme for calculating the nonlinear term. Hence, $N = \frac{2}{3}N^*$ for comparison.

$$\mathbf{a} = \nabla \Delta^{-1} \nabla \cdot (\mathbf{u} \cdot \nabla \mathbf{u}) + \hat{D}\mathbf{u}, \qquad (6)$$

where the first term is the pressure term written in terms of the nonlinear velocity term, and the second term is representative of dissipation.

The temporal derivative of the acceleration is calculated using second order central finite differences of the acceleration fields calculated at previous time steps. The spatial and temporal derivatives of $\mathbf{a}$ are needed to calculate the ZAP velocity $\mathbf{V_a}$.

To investigate whether observations are dependent on the ratio of outer and inner length scales, $\mathcal{L}/\eta$, we employ a low-pass filter with a cutoff wave number k_{cutoff} by multiplying the vorticity field with the Heaviside step function $\Theta(\cdot)$ before calculating all other derived quantities [37],

$$\omega_{\mathbf{k},\text{filtered}} = \Theta(k_{cutoff} - |\mathbf{k}|)\omega_{\mathbf{k},\text{DNS}}. \qquad (7)$$

The employed filtering wave numbers and names of the associated runs are detailed in Table II. Typical scales and other characteristic properties of the different runs are listed in Table III. Note that the highest filtering threshold $k_{cutoff} = N/2$ is equivalent to not filtering the vorticity field (unfiltered runs A2, B3, and C4). All other runs have the enstrophy cascade typical of two dimensional turbulence and the forcing scale $2\pi/k_f$ filtered out. Hence, aside from a varying ratio of outer to inner length scale, $\mathcal{L}/\eta$, there is a qualitative difference between the filtered and unfiltered runs: the filtered runs only contain the inverse energy cascade part of the energy spectrum (and the large-scale dissipation), while the unfiltered runs also contain the forcing and enstrophy cascade. We mainly focus on results relating to the inverse cas-

TABLE II. Labeling of DNS runs for different resolutions N and low-pass filtering cutoff wave number k_{cutoff}. Runs A2, B3, and C4 are essentially unfiltered as the cutoff wave number is equal to the highest wave number in spectral space.

	$N=256$	$N=512$	$N=1024$
$k_{cutoff}=64$	A1	B1	C1
$k_{cutoff}=128$	A2	B2	C2
$k_{cutoff}=256$		B3	C3
$k_{cutoff}=512$			C4

cade, and thus the filtered runs, but point out differences between the filtered and unfiltered runs where appropriate.

We use third order Lagrange interpolation to calculate the value of quantities at locations between grid points. In order to correctly resolve all quantities examined in this work, we make sure that the resolution we use for the interpolation and all intermediate steps is sufficient to accommodate the highest wave number features possible in Fourier space. The quantity with the highest possible nonvanishing wave number in this work is the determinant of the acceleration gradient tensor, which is of the order of square of $\nabla(\mathbf{u} \cdot \nabla \mathbf{u})$, and thus can have nonzero wave numbers up to four times as high as the velocity $\mathbf{u}$ and hence the vorticity ω, which is the basic quantity integrated in the DNS and thus defining the resolution N. Therefore, the resolution we employ to calculate other quantities is $N_a^2 = (4N)^2$. In the cases where the vorticity is low-pass filtered, $N_a^2 = (8k_{cutoff})^2$ is sufficient to resolve the highest wave number features of the $\det(\nabla \mathbf{a})$-field.

The zero acceleration points at a given time step are found by a combination of an Euler stepping [31] and the conventional Newton-Raphson method. The acceleration vectors at the corners of each grid cell are examined for a change of sign within the cell. An indication for a zero point within a cell is given when both vector components change sign in a grid cell. The approximate position of this zero point is determined by inverting a bilinear interpolation for the zero value. This point will act as the starting point for the iterative zero point-locating algorithm. The algorithm distinguishes between stable and unstable critical points in the following way; the former have a local acceleration field where all vectors point towards the ZAP, whereas the latter do not. Hence, if the zero point in question is stable, the actual acceleration vector at this initial position will point into the vicinity of the zero point, and subsequent iterations following this acceleration vector at each iteration will bring the current position closer to the actual zero point. If the zero point is not stable, the point can be stabilized by multiplying the acceleration field with a matrix whose elements are $\in \{0, \pm 1\}$, and each row and column contains only one nonzero element [31]. All such matrices are applied to the acceleration field in order to find all ZAPs irrespective of their stability. This procedure is repeated iteratively until the best guess position is either (1) accelerating its trajectory three

TABLE III. Typical scales of all DNS runs. $\mathcal{L}$ and η are the outer (i.e., integral) and inner length scale, respectively. $\eta = 2\pi/k_{\text{cutoff}}$ for filtered runs and $\eta = 5\pi/2k_{\text{cutoff}}$ for the unfiltered runs A2, B3, and C4. $\lambda = u'/(\partial u_1/\partial x)_{\text{rms}}$ and $\lambda_a = a'/(\partial a_1/\partial x)_{\text{rms}}$ are the Taylor microscale of the velocity and acceleration field, with $u' = \sqrt{\langle u_1 \rangle}$ and $a' = \sqrt{\langle a_1 \rangle}$ being the root mean squared velocity and acceleration 1-component of the flow. Note that $\lambda_a \approx 0.3\eta$. Throughout the paper, primes on quantities or the subscript "rms" denote the rms of that quantity over the entire flow. $u_\eta = (\eta\epsilon)^{1/3}$ is the characteristic small-scale velocity, where ϵ is the mean energy dissipation of the unfiltered flow. $(\nabla \cdot \mathbf{a})_{\text{rms}}$ and $\det(\nabla \mathbf{a})_{\text{rms}}$ are the rms of the two invariants of the acceleration gradient tensor and #ZAPs denotes the typical number of ZAPs to be found in the flow at an instant in time. The ratio between #ZAPs of different classes, as defined in Sec. IV B, is 26:24:50 for vortical, straining and anti-ZAPs in the filtered runs and 25:22:53 in the unfiltered runs A2, B3, and C4. All numbers are in DNS units and given with two significant figures.

Run	$\mathcal{L}$	η	λ	λ_a	u'	u_η	a'	ϵ	$\mathcal{L}/\eta$	$\nabla \cdot \mathbf{a}_{\text{rms}}$	$\det(\nabla \mathbf{a})_{\text{rms}}$	#ZAPs
A1	0.40	0.098	0.12	0.030	3.2	0.67	87	3.1	4.0	4800	22×10^6	5500
A2	0.38	0.061	0.089	0.019	3.3	0.57	120	3.1	6.2	9900	110×10^6	14000
B1	0.37	0.098	0.13	0.030	2.4	0.51	50	1.4	3.7	2800	6.7×10^6	5700
B2	0.35	0.049	0.078	0.015	2.5	0.41	70	1.4	7.1	7600	57×10^6	21000
B3	0.34	0.031	0.055	0.0095	2.5	0.35	91	1.4	11	15000	280×10^6	52000
C1	0.33	0.098	0.12	0.029	1.7	0.37	26	0.50	3.4	1400	1.7×10^6	5900
C2	0.31	0.049	0.075	0.015	1.7	0.29	36	0.50	6.4	3800	13×10^6	22000
C3	0.30	0.025	0.046	0.0074	1.8	0.23	50	0.50	12	11000	130×10^6	83000
C4	0.30	0.015	0.032	0.0047	1.8	0.20	67	0.50	19	23000	640×10^6	200000

consecutive times ("run-away"), (2) leaving the grid cell, (3) reaching the 100th iteration, or (4) reaching a value of acceleration which is equal to $a_{\text{rms}}/20$. In the former three cases, the iteration is aborted and the next stabilizing matrix is tried until all eight matrices have been tried. In the latter case, the best guess is now sufficiently close to the ZAP to initiate a Newton-Raphson search. Five Newton-Raphson iterations are usually sufficient to bring the magnitude of acceleration at the best guess ZAP down to $a_{\text{rms}}/10^6$. Only points that satisfy this last criterion are being considered close enough to zero value to pose as ZAPs for the purpose of this paper.

Once the ZAPs are found at individual time steps, we need to match them at different time steps to create ZAP trajectories. To achieve this, all ZAP positions, $\mathbf{x}_a(t)$, at a certain time step, say t_0, are advanced by their velocity which is calculated from Eq. (3),

$$\mathbf{x}_{a,\text{guess}}(t_1) = \mathbf{x}_a(t_0) + \mathbf{V}_a(t_0)dt, \qquad (8)$$

to give a guess for the position at the next time step, t_1, where $dt = t_1 - t_0$. We can then match the nearest neighbors between all ZAPs at time t_1 and the guessed positions from the advanced t_0-ZAPs, with a threshold of $2\pi/(10N_a)$ (i.e., a tenth of a grid cell) for the maximum distance between them. Points that have a nearest neighbor belong to the same trajectory. Points in the set of ZAPs at t_1 which do not have a nearest neighbor within this threshold are considered to be newly created, and hence beginnings of new trajectories. Neighborless points in the set of advanced guesses from t_0 are considered destroyed and thus mark the end of a trajectory.

The ZAP trajectories are then stored on the hard disk for postprocessing along with the ZAP velocity $\mathbf{V}_a$, $\det(\nabla \mathbf{a})$, $\nabla \cdot \mathbf{a}$, and the fluid velocity $\mathbf{u}$ at every ZAP.

The various thresholds and parameters involved in finding the ZAPs numerically have been adjusted to yield a high number of ZAPs with the most restrictive threshold being the upper limit of $a_{\text{rms}}/10^6$ for the absolute value of acceleration at a ZAP. The remaining thresholds and parameters have been chosen to be loose enough to gain the maximum amount of ZAPs while being as restrictive as possible when a loosening of the threshold did not increase the number of ZAPs significantly. However, it is also unavoidable that a small amount of ZAPs are not detected, which may lead to gaps in trajectories, or undetected trajectories altogether. Furthermore, false positives, i.e., points that have an absolute value of acceleration smaller than $a_{\text{rms}}/10^6$, but not exactly zero, are probably also present in the data, most likely manifested in very short trajectories or singular ZAPs ("blips").

Aside from choosing suitable parameters and thresholds, we have taken some additional measures to address these issues. Very short trajectories with a length of one or two time steps are excluded from the statistics and obvious gaps in the trajectories are filled with linear interpolations of ZAP positions and other recorded quantities. The method we employ to identify gaps is outlined in the appendix.

The basic tool we employ for statistical analysis is the conditional (and joint) probability density function (PDF). The relationship of two quantities is explored by recording the PDFs of one quantity for a set of given values of the second (conditional) quantity along with the first few moments of the PDF.

IV. CLASSIFICATION OF ZAPS

We find that the two-dimensional turbulence used in this work exhibits the same characteristic relation between the rms pressure gradient and dissipation term of the entire fluid as found in three-dimensional turbulence [32,33], see Fig. 2 [38],

$$(\nabla p)_{\text{rms}} \gg (\hat{D}\mathbf{u})_{\text{rms}}. \qquad (9)$$

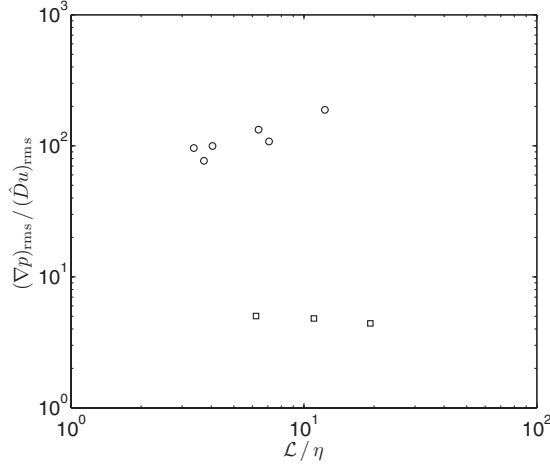FIG. 2. Ratio of rms pressure gradient, $(\nabla p)_{\mathrm{rms}}$, and dissipation term, $(\hat{D}\mathbf{u})_{\mathrm{rms}}$, of entire DNS flow. The unfiltered runs A2, B3, and C4 are marked with a square ($\square$), the remaining filtered runs with a circle ($\bigcirc$). In all cases $(\nabla p)_{\mathrm{rms}} \gg (\hat{D}\mathbf{u})_{\mathrm{rms}}$.

However, this does not imply that ∇p dominates over $\hat{D}\mathbf{u}$ at ZAPs because ZAPs are points where the balance $\nabla p = \hat{D}\mathbf{u}$ holds.

In fact, the PDF of $|\nabla p(\mathbf{x_a})|$, taken at all ZAPs $\mathbf{x_a}$ only (Fig. 3), shows clearly that none of the ZAPs are pressure extrema. In particular, the peak of this distribution is sufficiently well represented by the rms pressure gradient conditioned on ZAPs only, $[\nabla p(\mathbf{x_a})]_{\mathrm{rms}}$, which is found to equal the rms dissipation term of the entire flow, $[\hat{D}\mathbf{u}(\mathbf{x})]_{\mathrm{rms}}$, i.e.,

$$\frac{[\nabla p(\mathbf{x_a})]_{\mathrm{rms}}}{[\hat{D}\mathbf{u}(\mathbf{x})]_{\mathrm{rms}}} = (0.997 \pm 0.014) = 1, \qquad (10)$$
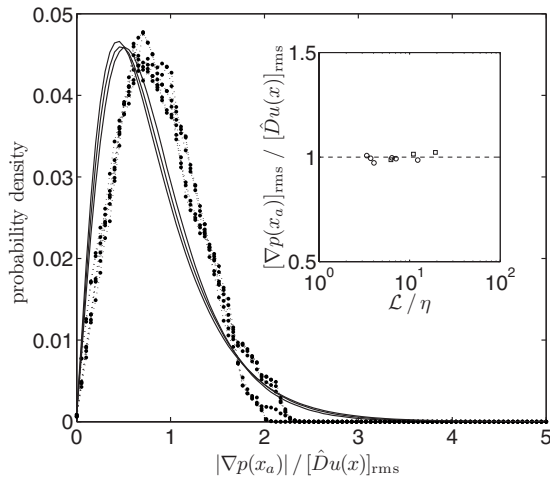

FIG. 3. PDFs of absolute value of pressure gradient at ZAPs only, $|\nabla p(\mathbf{x_a})|$. The solid lines are the unfiltered runs A2, B3, and C4, the bullets ($\bullet$) and dotted lines are the remaining filtered runs. Inset: ratio of rms pressure gradient at ZAPs only, $[\nabla p(\mathbf{x_a})]_{\mathrm{rms}}$, and dissipation term of entire DNS flow, $[\hat{D}\mathbf{u}(\mathbf{x})]_{\mathrm{rms}}$. The unfiltered runs are marked with a square ($\square$), the filtered runs with a circle ($\bigcirc$). The dashed line is the constant 1.

where the position vector $\mathbf{x_a}$ indicates that the rms value is obtained at ZAPs only, while $\mathbf{x}$ refers to values sampled from the entire flow (see Fig. 3).

In summary, using $\nabla p(\mathbf{x_a}) = \hat{D}\mathbf{u}(\mathbf{x_a})$,

$$[\nabla p(\mathbf{x_a})]_{\mathrm{rms}} = [\hat{D}\mathbf{u}(\mathbf{x_a})]_{\mathrm{rms}} \approx [\hat{D}\mathbf{u}(\mathbf{x})]_{\mathrm{rms}} \ll [\nabla p(\mathbf{x})]_{\mathrm{rms}}, \qquad (11)$$

for both filtered and unfiltered runs, despite the vastly different values of the ratio $[\nabla p(\mathbf{x})]_{\mathrm{rms}}/[\hat{D}\mathbf{u}(\mathbf{x})]_{\mathrm{rms}}$ plotted in Fig. 2, suggesting that Eq. (11) is universally true for flows with arbitrary such ratios.

Thus, ZAPs are not only different from pressure extrema, they are also points where the value of $\hat{D}\mathbf{u}$ is nonzero and in fact fluctuates as much as over the entire flow. It is $[\hat{D}\mathbf{u}(\mathbf{x})]_{\mathrm{rms}}$ which determines the strength of these fluctuations and of those of ∇p on ZAPs.

A. Observations of the acceleration gradient tensor

Our classification of ZAPs and their neighborhoods relies on the following three observations concerning the acceleration gradient tensor at and in the neighborhood of ZAPs.

(i) The asymmetric part of the acceleration gradient tensor is very small compared to the symmetric part for sufficiently large determinants of $\nabla \mathbf{a}$, and small in general.

In this 2D turbulence, the symmetric and antisymmetric gradient tensors are given by

$$\partial_{(_i}a_{j)} = -\partial_{ij}p + \hat{D}s_{ij}, \qquad (12)$$

$$\partial_{[_i}a_{j]} = \frac{1}{2}\epsilon_{ijl}\hat{D}\omega_l, \qquad (13)$$

where we employed the Einstein summation convention, the round and square brackets denote symmetrization and antisymmetrization, $s_{ij} = \partial_{(_i}u_{j)}$ is the strain tensor, ϵ_{ijl} is the Levi-Civita symbol and ω_l is the vorticity.

Knowing Eq. (9), it is not surprising that the pressure Hessian, $\partial_{ij}p$, should on average dominate the gradient of the viscous term, $\partial_i \hat{D}u_j$, and thus,

$$[\partial_{[_i}a_{j]}]_{\mathrm{rms}} \ll [\partial_{(_i}a_{j)}]_{\mathrm{rms}}, \qquad (14)$$

as shown in Fig. 5 where we used the Frobenius norm for matrices to calculate the rms values.

Consequently,

$$\det(\nabla \mathbf{a}) \approx \det(\nabla \mathbf{a}^{(s)}), \qquad (15)$$

where now the superscript "(s)" denotes the symmetric part of the tensor. Note that in the low-pass filtered runs, the antisymmetric part essentially vanishes completely, and in the unfiltered runs A2, B3, and C4, it is still small with 60% of all ZAPs having $|\det(\nabla \mathbf{a}^{(as)})/\det(\nabla \mathbf{a}^{(s)})| < 0.1$, see Fig. 4.

The difference between the filtered and unfiltered runs in Figs. 4 and 5, is due to the fact that the high-wave number part of the spectrum contains almost all contributions to the viscous term and hence, filtering that part out implies by Eq.
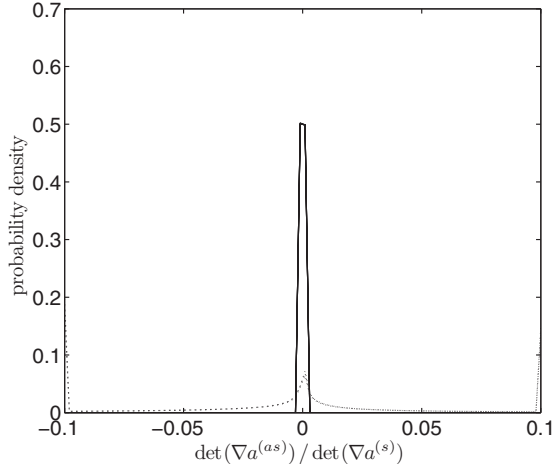
FIG. 4. Probability density function (PDF) of the ratio between the determinant of the asymmetric and symmetric part of the acceleration gradient tensor at ZAPs. All low-pass filtered runs collapse on the solid black line. The unfiltered runs A2, B3, and C4 collapse on the dotted line. Over 60% of all ZAPs in the unfiltered runs have $|\det(\nabla \mathbf{a}^{(as)})/\det(\nabla \mathbf{a}^{(s)})| < 0.1$. These PDFs look identical when obtained from sampling the entire flow.

(13) that $\partial_{[i}a_{j]} \approx 0$. This effect is further amplified by the hyperviscous term in the dissipation operator $\hat{D}$, which is of order Δ^8 (or k^{16} in Fourier space).

The classification of ZAPs which we introduce in the following subsection Sec. IV B relies on Eq. (15). It is therefore a nearly complete classification of those ZAPs which are not directly influenced by the dissipative high wave number part of the spectrum, so that the antisymmetric part of $\nabla \mathbf{a}$ is negligible and thus, the imaginary part of the eigenvalues of $\nabla \mathbf{a}$
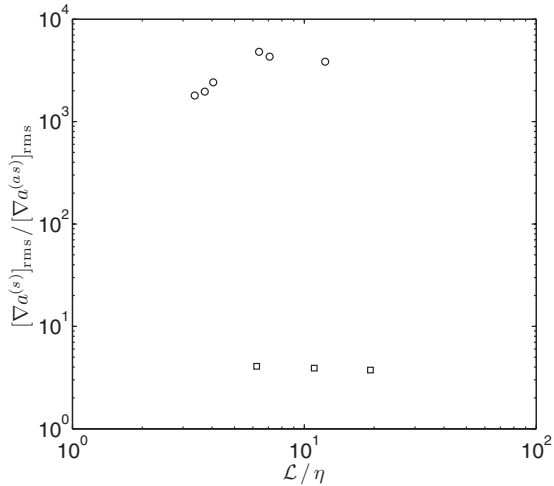

FIG. 5. Ratio of symmetric to antisymmetric rms acceleration gradient tensor, $[\nabla \mathbf{a}^{(s)}]_{rms}/[\nabla \mathbf{a}^{(as)}]_{rms}$, of entire DNS flow. The superscripts "(s)" and "(as)" denote the symmetric and antisymmetric part of the tensor, respectively. The Frobenius norm for matrices is used to calculate the rms values. The unfiltered runs A2, B3, and C4 are marked with a square ($\square$), the remaining filtered runs with a circle ($\bigcirc$). In all cases $[\nabla \mathbf{a}^{(s)}]_{rms} \gg [\nabla \mathbf{a}^{(as)}]_{rms}$.
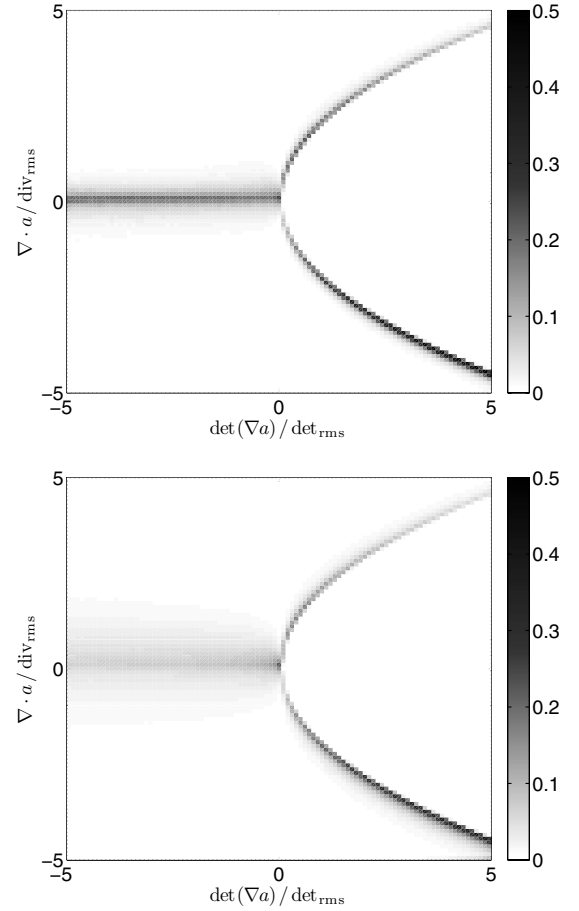

FIG. 6. Pitchfork diagram: (Top) This is a conditional PDF of $\nabla \cdot \mathbf{a}$ conditioned on $\det(\nabla \mathbf{a})$ for all ZAPs of run C3. Every column in the diagram is a normalized PDF conditioned on (c/o) the value of $\det(\nabla \mathbf{a})$ given on the x axis. The color gives the height of the PDF. The PDFs are peaked at $\nabla \cdot \mathbf{a} = 0$ for negative $\det(\nabla \mathbf{a})$ and exhibit two peaks for $\det(\nabla \mathbf{a}) > 0$. The position of the peaks implies that the eigenvalues of ZAPs with $\det(\nabla \mathbf{a}) > 0$ are approximately degenerate. (Bottom) This is the same conditional PDF as shown on top, now for all grid points in run C3. It is very similar to the top figure, with less pronounced peaks in the PDFs. Both figures are qualitatively the same in all runs, filtered and unfiltered.

is also negligible. The eigenvalues γ of the two-dimensional acceleration gradient tensor are therefore approximately real in that case and given by

$$\gamma \approx \frac{1}{2}\{\nabla \cdot \mathbf{a} \pm \sqrt{(\nabla \cdot \mathbf{a})^2 - 4\det[\nabla \mathbf{a}^{(s)}]}\}. \qquad (16)$$

The following two observations are given in the context where Eq. (15) holds in preparation for the ZAP classification in Sec. IV B.

(ii) The PDF of $\nabla \cdot \mathbf{a}$ conditioned on (c/o) $\det(\nabla \mathbf{a}^{(s)})$ is peaked at zero for $\det(\nabla \mathbf{a}^{(s)}) < 0$, see Fig. 6.

(iii) The eigenvectors γ are approximately degenerate for positive $\det(\nabla \mathbf{a}^{(s)})$,

$$\det(\nabla \mathbf{a}^{(s)}) \lesseqgtr \frac{1}{4}(\nabla \cdot \mathbf{a})^2. \qquad (17)$$
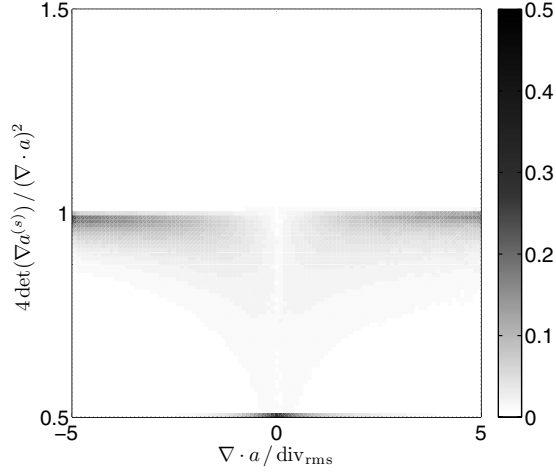
FIG. 7. Positive $\det(\nabla \mathbf{a}^{(s)})$ part of pitchfork diagram (fig. 6), compensated for Eq. (17): shown is a conditional PDF of $4 \det(\nabla \mathbf{a}^{(s)})/(\nabla \cdot \mathbf{a})^2$ c/o $\nabla \cdot \mathbf{a}$ and $\det(\nabla \mathbf{a}^{(s)}) > 0$ for all ZAPs of run C3. This figure is qualitatively the same in all runs, filtered and unfiltered.

That is, $\det(\nabla \mathbf{a}^{(s)}) \approx (\nabla \cdot \mathbf{a})^2/4$ throughout the right hand branches seen in Fig. 6, and deviations from this approximate equality are always such that $\det(\nabla \mathbf{a}^{(s)}) < (\nabla \cdot \mathbf{a})^2/4$. This is clearly illustrated in Fig. 7. As a consequence,

$$\nabla \cdot \mathbf{a} = 0 \Rightarrow \det(\nabla \mathbf{a}^{(s)}) \lessgtr 0, \qquad (18)$$

which establishes the separation of the two peaks in the PDF of $\nabla \cdot \mathbf{a}$ c/o $\det(\nabla \mathbf{a}^{(s)}) > 0$ as seen in Fig. 6.

These observations apply to acceleration gradient tensors at ZAPs, and also to the entire flow field, albeit with less degenerate eigenvalues, as shown in Fig. 6.

B. Proposed classification

To understand the different branches in Fig. 6, let us consider the relation between the acceleration and the velocity field of incompressible fluids. Taking the divergence of the Navier-Stokes equation and using incompressibility, one arrives at

$$\partial_i a_i = (\partial_i u_j)(\partial_j u_i) = -2Q, \qquad (19)$$

where Q is the second invariant of the velocity gradient tensor. In two dimensions, Eq. (19) is also equal to the determinant of the velocity gradient tensor. Furthermore, for divergence-free velocity fields, the eigenvalues of the velocity gradient tensor are either real or imaginary. Hence, the sign of the divergence of the acceleration field is directly linked to the nature of the eigenvalues of the velocity gradient tensor.

The three distinct branches in Fig. 6 prompt the following classification given by the value of the acceleration gradient tensor at a ZAP,

Vortical ZAPs:$\det(\nabla \mathbf{a}^{(s)}) > 0$; $\quad \nabla \cdot \mathbf{a} < 0$.

Due to the degenerate nature of the eigenvalues of $\nabla \mathbf{a}$, the local acceleration field around the ZAP is isotropic and the negative divergence indicates that the acceleration vectors point towards the ZAP. By Eq. (19) this implies that the velocity gradient tensor has imaginary eigenvalues which corresponds to solid body rotation of the flow field in the immediate neighborhood of the ZAP.

Straining ZAPs:$\det(\nabla \mathbf{a}^{(s)}) > 0$; $\quad \nabla \cdot \mathbf{a} > 0$.

Following the same arguments, the acceleration field is locally isotropic with vectors pointing away from the ZAP. The velocity gradient tensor has real eigenvalues and thus, the flow field is locally straining.

Anti-ZAPs:$\det(\nabla \mathbf{a}^{(s)}) < 0$.

The square root in Eq. (16) cannot vanish and hence, the eigenvalues of $\nabla \mathbf{a}$ are not degenerate. We cannot make a definitive statement about the nature of the velocity field in this case. The name *anti-ZAP* is chosen in analogy to elementary particles, because ZAPs (in this context meaning vortical and straining only) and anti-ZAPs are created and annihilated in pairs, similar to, e.g., electrons and their antiparticles, positrons. Furthermore, anti-ZAPs exhibit behavior which is qualitatively distinct from that of vortical and straining ZAPs as will become clear throughout the remainder of this paper.

There is about the same number of vortical and straining ZAPs and about 50% of all ZAPs are anti-ZAPs (see caption of Table III). These proportions are consistent with the fact that ZAPs are created and destroyed in pairs of one vortical or straining ZAP and one anti-ZAP.

The classification in terms of vortical, straining and anti-ZAPs is nearly exhaustive in the case of filtered runs where Eq. (15) holds at the vast majority of ZAPs. An exhaustive classification of ZAPs in the unfiltered runs would need to account for the remaining minority of ZAPs which are directly related to the high-wave number dissipation range of the energy spectrum and which are characterized by complex eigenvalues of the acceleration gradient tensor. This issue is beyond this paper's scope and we leave it for future study.

V. SWEEPING OF ZAPS

A ZAP is perfectly swept by the fluid flow when its velocity $\mathbf{V_a}$ equals the fluid velocity $\mathbf{u}$ at its location $\mathbf{x_a}$,

$$\xi(\mathbf{x_a}) \equiv \mathbf{u}(\mathbf{x_a}) - \mathbf{V_a}(\mathbf{x_a}) = 0, \qquad (20)$$

where we also defined the local fluid velocity in the ZAP frame, $\xi(\mathbf{x_a})$. However, perfect sweeping cannot be sustained for a prolonged time as the only motion admitted by perfect sweeping is that the ZAP (and hence the fluid element at the ZAP) moves in a straight line with constant speed [39].

We therefore consider sweeping in a statistical sense to be observed when there are statistical correlations between $\mathbf{u}$ and $\mathbf{V_a}$ such that the absolute value of ξ is much smaller than u'.

A. Correlation and decorrelation of u, Vₐ, and ξ

Following the ways data were presented in [34] we explore the correlation between the fluid velocity $\mathbf{u}$, ZAP velocity $\mathbf{V_a}$ and the local fluid velocity ξ using joint PDFs of
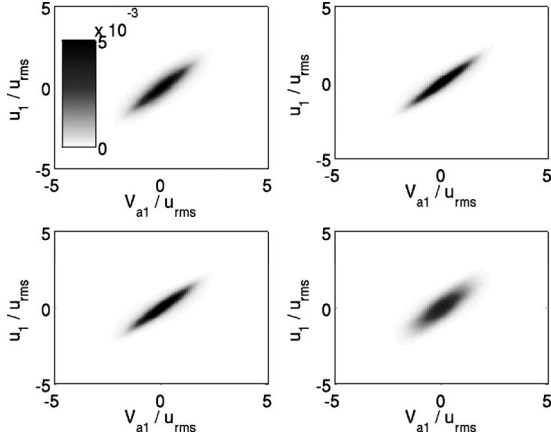
FIG. 8. Joint PDFs of u_1 and V_{a1} at ZAPs of run C3. The strong direct correlation visible in the plot of all ZAPs (top left) is even more pronounced in the joint PDFs of vortical (top right) and straining ZAPs (bottom left). The plot for the anti-ZAPs (bottom right) shows a weaker correlation. All plots in Figs. 8–10 are representative of all runs.

the vectors' one-component. Since the flow is isotropic and no preferential direction is singled out by the vanishing acceleration at ZAPs, these joint PDFs give a good indication of the correlation between the actual vectors.

In addition to the analysis carried out by [34], we will also present joint PDFs of different ZAP classes to highlight their differences. The strong direct correlation of **u** and **V$_a$** visible in the plot of all ZAPs in Fig. 8 is even more pronounced in the joint PDFs of vortical and straining ZAPs, suggesting better sweeping for these ZAP classes. The plot for the anti-ZAPs shows a weaker correlation of **u** and **V$_a$**.

Fig. 9 shows the decorrelation between ξ and **u** for vortical and straining ZAPs, and a weak correlation for anti-ZAPs. Note also that in the former two cases, the width of the PDF is much smaller for ξ than it is for **u**, thus indicating further evidence of sweeping for these ZAPs.

The decorrelation between ξ and **V$_a$** is approximately visible in all three classes, as shown in Fig. 10. Again, the better
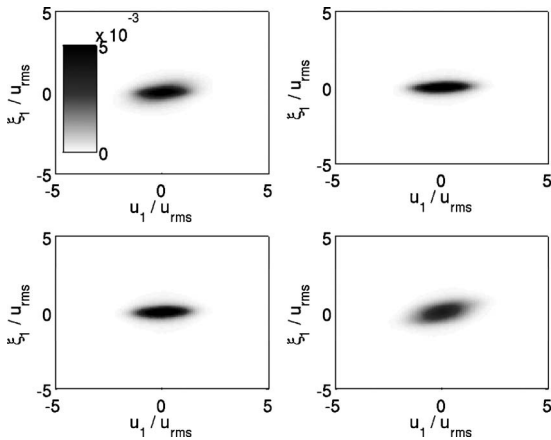

FIG. 9. Joint PDFs of ξ_1 and u_1 at ZAPs of run C3. The decorrelation visible in the plot of all ZAPs (top left) is clearer in the joint PDFs of vortical (top right) and straining ZAPs (bottom left). The plot for the anti-ZAPs (bottom right) shows a weak correlation instead.
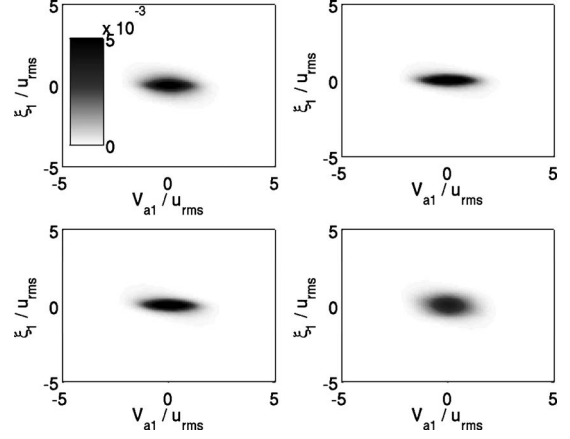

FIG. 10. Joint PDFs of ξ_1 and V_{a1} at ZAPs of run C3. The decorrelation is visible in all plots (clockwise from top left: all ZAPs, vortical, anti-ZAPs and straining). There is a faint anticorrelation noticeable for large values of $|V_{a1}|$, most visible for anti-ZAP (bottom right). This is expected from (20).

sweeping of the vortical and straining ZAPs is indicated by a narrower peak of the PDF along the ξ_1 axis. The anticorrelation which is faintly visible for large values of $|V_{a1}|$, and best seen for anti-ZAPs, must exist when $|\mathbf{u}| \ll |\mathbf{V_a}|$ due to the definition of ξ, Eq. (20). This is expected to occur near creation or destruction events (see Sec. II B).

The observations made by [34] for all ZAPs can now be confirmed for the vortical and straining ZAPs. However, the anti-ZAPs show a slightly different behavior, most notably that anti-ZAPs exhibit a weak correlation between ξ and **u** and furthermore, are not swept as well as vortical and straining ZAPs.

B. rms of ξ along ZAP trajectories

Sweeping is persistence in the Lagrangian frame, and as such it is not an instantaneous phenomenon. Hence, we now want to explore the sweeping behavior not just at instantaneous ZAPs, but in relation to whole ZAP trajectories, which have been obtained as described in Sec. III.

As a measure of sweeping of a ZAP over its entire lifetime, we consider the root mean squared ξ at a ZAP, averaged over its lifetime, sampled at every recorded time step of its trajectory. There are a few caveats that need to be considered.

Firstly, as detailed in Sec. II B, the creations and destructions of ZAPs happen when $\det(\nabla\mathbf{a})=0$, which means that at these events, $|\mathbf{V_a}| \to \infty$ and thus also $|\xi| \to \infty$. We define the rms of ξ averaged over a ZAP's trajectory,

$$\xi'_{\text{traj}} \equiv \sqrt{\langle \xi^2 \rangle_{\text{traj}}} = \sqrt{\frac{1}{T_{\text{life}}} \int_0^{T_{\text{life}}} \xi^2(t')\mathrm{d}t'}, \qquad (21)$$

with T_{life} being the lifetime of the particular ZAP trajectory considered, and $\langle \cdot \rangle_{\text{traj}}$ indicating the average over that single trajectory (the subscript "traj" indicates that a quantity refers to a single trajectory). ξ'_{traj} is not necessarily well defined, as the boundaries of the averaging domain are singularities and we do not have sufficient knowledge about the behavior of
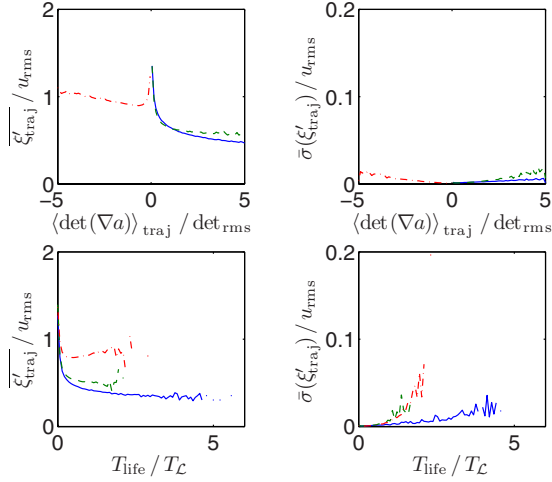
FIG. 11. (Color online) Means of ξ'_{traj} from all trajectories in run C3 (left column) and their standard deviation (right column). The top row is conditioned on the trajectory average of the determinant of the acceleration gradient tensor, $\langle \det(\nabla \mathbf{a}) \rangle_{\text{traj}}$. The bottom row is conditioned on the trajectories' lifetimes. Shown are vortical ZAPs only (solid blue line), straining ZAPs only (dashed green) and anti-ZAPs only (dash-dotted red). The means are sampled from all recorded ZAP trajectories in a simulation run. The standard deviation $\bar{\sigma}$ is the square root of the variance of all ξ'_{traj} contributing to a PDF (Var), divided by the number (n) of sampled ξ'_{traj}: $\bar{\sigma} = \sqrt{\text{Var}/n}$. Extreme trajectories with $\xi'_{\text{traj}} > 5u'$ have been disregarded for these plots to avoid cluttering peaks. These plots are qualitatively representative of all runs.

$|\xi|$ near these singularities. However, if one assumes that the singularity is well behaved in the sense that Eq. (21) is finite, this average can be calculated using a finite amount of sampling points.

Secondly, since we want to use Eq. (21) as a measure of sweeping for a ZAP trajectory, we are not primarily interested in the contribution of the singularities to the average, but in the typical value of ξ^2 at the ZAP when it is not being created or destroyed. As before, we expect typically $|\xi(\mathbf{x})| < u'$ at positions $\mathbf{x}$ where sweeping takes place along a trajectory. However, it is difficult to select and disregard the contributions of the creation and destruction events to the average. Thus, we average over the entire trajectory (where this is possible, see next paragraph) and acknowledge that the singularities at the beginning and end of a trajectory will introduce a "lifetime-bias" that gives higher values to ξ'_{traj} for shorter lived trajectories. Taking this into account, the values arising from this kind of averaging can only be used for qualitative comparisons of sweeping.

Lastly, the numerical method employed to find the trajectories cannot guarantee that the trajectory will contain the singularity at the beginning and the end. This might be either because the ZAP was created in the flow before we started to record trajectories (or is destroyed only after we stop recording) or because the trajectory tracking is interrupted due to numerical issues (see Sec. III). This means that the lifetime-bias might not be present for some trajectories at random.

Taking these issues into account, in Fig. 11 we plot $\overline{\xi'_{\text{traj}}}$, a mean ξ'_{traj} over particular sets of trajectories in a run. In the

top row of Fig. 11 we calculate this mean by conditioning these trajectories on $\langle \det(\nabla \mathbf{a}) \rangle_{\text{traj}}$ and see that, generally, $\overline{\xi'_{\text{traj}}} < u'$ for positive $\langle \det(\nabla \mathbf{a}) \rangle_{\text{traj}}$. That is, sweeping is present for vortical and straining ZAP trajectories. However, $\overline{\xi'_{\text{traj}}} \gtrsim u'$ for negative $\langle \det(\nabla \mathbf{a}) \rangle_{\text{traj}}$, i.e. no evidence of sweeping can be found for anti-ZAP trajectories.

Furthermore, the bottom row of plots in Fig. 11 clearly shows the lifetime-bias of ξ'_{traj} for short-lived trajectories, which are dominated by creation and destruction events. In these cases when the lifetime is short, we expect sweeping to only take place for a small fraction of the ZAP's lifetime, if at all. Moreover, the bottom row of plots in Fig. 11 also shows that the long-lived vortical and straining trajectories are well swept, with the vortical ones having the lowest $\overline{\xi'_{\text{traj}}}$.

Summarizing, we found evidence for sweeping of long-lived vortical and straining ZAPs and no indication that anti-ZAPs are swept, irrespective of their lifetime. Sweeping of short-lived (vortical and straining) ZAPs cannot be observed; however a very short period of sweeping cannot be ruled out completely.

C. Reynolds number dependence of sweeping

Chen *et al.* [24] presented a scaling argument for ξ_{rms} which we repeat and discuss within the context of our own different results. Equation (2) can easily be transformed into

$$\frac{D\mathbf{a}}{Dt} = \xi \cdot \nabla \mathbf{a}, \tag{22}$$

where D/Dt denotes the Lagrangian derivative following the fluid velocity $\mathbf{u}$. Assuming statistical independence of ξ and $\nabla \mathbf{a}$ as well as Kolmogorov scaling at ZAPs, that is all Lagrangian and spatial derivatives of $\mathbf{a}$ at ZAPs scale as small-scale quantities, Chen *et al.* [24] argued that

$$\xi' \equiv \sqrt{\langle \xi^2 \rangle} \sim \frac{(D\mathbf{a}/Dt)_{\text{rms}}}{(\nabla \mathbf{a})_{\text{rms}}} \sim \frac{\eta}{\tau_\eta} \sim u_\eta, \tag{23}$$

where $\langle \cdot \rangle$ is the average over all ZAPs at an instant in time and η and τ_η are, respectively, the length- and time-scale of the smallest eddies in the flow. For the filtered data we expect $u_\eta \sim u'(\mathcal{L}/\eta)^{-1/3}$ by virtue of its well-defined energy spectrum $\propto k^{-5/3}$ [16].

The conclusion is that ZAPs move on average like a small-scale quantity proportional to the small-scale velocity u_η. However, our filtered data are best fitted with the scaling

$$\xi' \sim u' \left(\frac{\mathcal{L}}{\eta} \right)^{-(0.257 \pm 0.008)} \approx u' \left(\frac{\mathcal{L}}{\eta} \right)^{-1/4}, \tag{24}$$

as can be seen in Fig. 12. While this might initially seem contrary to the scaling suggested by Chen *et al.* [24], let us apply the discussion of ξ'_{traj} in Sec. V B.

ZAPs which are sufficiently close to creation or destruction will have a very large (instantaneous) $|\xi|$. Let us refer to such ZAPs as being in a *near-singular state*. Following the arguments in Sec. V B, ZAPs with short trajectories are predominantly in a near-singular state. On the other hand, we shall define ZAPs which have a very small $|\xi|$ as being in a *swept state*. In Sec. V B, we have seen that sufficiently long-
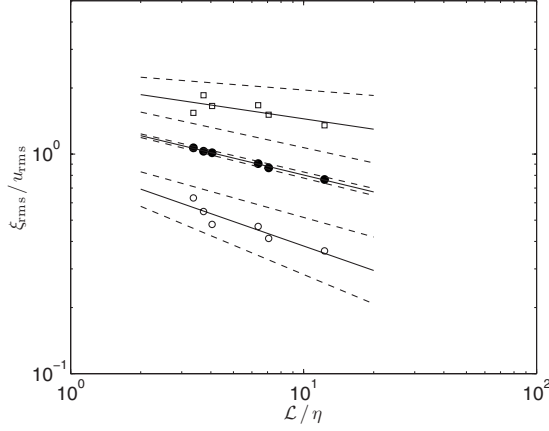
FIG. 12. Reynolds number dependence of ξ' at ZAPs and trajectories. Shown are: the average ξ'_{traj} of all trajectories in a run sampled over trajectories of all ZAPs with a lifetime $T_{\mathrm{life}} \in [0, 0.05] T_{\mathcal{L}}$ (squares $\square$) and sampled over trajectories of vortical ZAPs with $T_{\mathrm{life}} \in [2, 4] T_{\mathcal{L}}$ (circles $\bigcirc$) as well as ξ' at all ZAPs (bullets $\bullet$). Extreme values with $|\xi| > 5u'$ have been filtered out to reduce the noise; $\eta = 2\pi/k_{\mathrm{cutoff}}$ in all cases. The solid lines are the best fit power law $\sim (\mathcal{L}/\eta)^p$ in every case and the dashed lines indicate the 1σ confidence interval of each fit. The best fit exponents are $p(\square) = -(0.158 \pm 0.075)$, $p(\bigcirc) = -(0.371 \pm 0.074)$, and $p(\bullet) = -(0.257 \pm 0.008)$. Filtered runs (A1, B1, B2, C1, C2, and C3) only.

lived vortical and straining ZAPs are mostly in this state.

With regards to our scaling argument, ZAPs which are not in a near-singular state should scale as $\xi' \sim u_\eta$ Eq. (23). For ZAPs in a *singular state*, i.e., at creation and destruction, we know that $|\xi| \approx |\mathbf{V_a}| \rightarrow \infty$ and hence, it is not feasible to suggest a meaningful scaling for singular or near-singular ZAPs.

However, it is clear that $\xi'_{\mathrm{near-singular}}$, which is obtained by sampling only near-singular ZAPs, should always be larger than ξ'_{swept} sampled at swept ZAPs only. When considering sweeping of all ZAPs irrespective of their state, one would expect $\xi'_{\mathrm{all}} \equiv \xi'$ to lie in between the extreme cases,

$$\xi'_{\mathrm{swept}} < \xi'_{\mathrm{all}} < \xi'_{\mathrm{near-singular}}. \tag{25}$$

These inequalities are valid for all $\mathcal{L}/\eta$ and hence, the scaling exponents must follow the inequalities

$$p_{\mathrm{swept}} \lesssim p_{\mathrm{all}} \lesssim p_{\mathrm{near-singular}}, \tag{26}$$

if a power-law of the form

$$\xi'_{\mathrm{state}} \sim \left(\frac{\mathcal{L}}{\eta} \right)^{p_{\mathrm{state}}} \tag{27}$$

is a reasonable approximation for all states, swept, near-singular or mixed together (all). Otherwise, Eq. (25) would be violated as $\mathcal{L}/\eta \rightarrow \infty$.

To verify these scalings, we estimate each ξ'_{state} by averaging over many appropriate ξ'_{traj} samples. To sample ZAPs in a predominantly near-singular state, we average over trajectories of all ZAP classes with $0 < T_{\mathrm{life}} < 0.05 T_{\mathcal{L}}$, i.e.,

$$\xi'_{\mathrm{near-singular}} \approx \langle \xi'_{\mathrm{traj}}(T_{\mathrm{life}}) \rangle_{T_{\mathrm{life}} \in [0, 0.05] T_{\mathcal{L}}}. \tag{28}$$

To sample ZAPs in a predominantly swept state we average over vortical ZAP trajectories with $2T_{\mathcal{L}} < T_{\mathrm{life}} < 4T_{\mathcal{L}}$, i.e.,

$$\xi'_{\mathrm{swept}} \approx \langle \xi'_{\mathrm{traj}}(T_{\mathrm{life}}) \rangle_{T_{\mathrm{life}} \in [2, 4] T_{\mathcal{L}}}. \tag{29}$$

In the latter case, we choose vortical ZAPs only as they are the only class of ZAP which provide statistics of sufficient quality for this scaling analysis at such long lifetimes. $T_{\mathcal{L}} = \mathcal{L}/u'$ is the integral timescale.

Figure 12 shows that the best fit power laws for all filtered runs are

$$\xi'_{\mathrm{near-singular}} \sim u' \left(\frac{\mathcal{L}}{\eta} \right)^{-(0.158 \pm 0.075)} \approx u' \left(\frac{\mathcal{L}}{\eta} \right)^{-1/8}, \tag{30}$$

obtained from the very short-lived trajectories and

$$\xi'_{\mathrm{swept}} \sim u' \left(\frac{\mathcal{L}}{\eta} \right)^{-(0.371 \pm 0.074)} \approx u' \left(\frac{\mathcal{L}}{\eta} \right)^{-1/3}, \tag{31}$$

from the long-lived vortical trajectories. The best fit slope in Eq. (30) is sensitive to the upper lifetime limit chosen for the approximating average; the current upper limit has been empirically chosen to minimize the uncertainty in the fit parameters. The best fit slope of Eq. (31) is robust with respect to small changes of the lifetime limits.

Given the uncertainty in the data and the arbitrariness of the chosen lifetime limits for averaging, we feel that these results offer a satisfactory confirmation of our arguments and the scaling behavior of local ZAP velocities ξ in the various ZAP states.

Our arguments, thus confirmed, show how ξ' of ZAPs in all states can scale with an exponent of $\mathcal{L}/\eta$ which is shallower than the initially expected $-1/3$. Indeed, we have seen that $p_{\mathrm{swept}} \approx -1/3$, which is a confirmation that $\xi'_{\mathrm{swept}} \sim u_\eta$.

The difference between Eq. (24) and the results presented in [24] is most likely due to the different algorithms employed to numerically find the ZAPs in the acceleration field, possibly introducing a different bias toward ZAPs in different states.

Aside from the subtle issues concerning the precise numerical value of the scaling exponent, the most important result is consistently found,

$$\frac{\xi'}{u'} \rightarrow 0 \quad \mathrm{as} \quad \frac{\mathcal{L}}{\eta} \rightarrow \infty, \tag{32}$$

which states that for increasing Reynolds numbers, ZAPs are on average more and more closely swept with the local fluid velocity $\mathbf{u}$, thus quantifying the Tennekes sweeping hypothesis [24,34,35].

VI. LIFETIME OF ZAP TRAJECTORIES

The effects that ZAPs may have on scalar mixing, velocity field dynamics and preferential concentration of inertial particles will surely depend on their lifetime. The PDF of trajectory lifetimes takes the same basic form in all runs. The histograms of lifetimes for the three ZAP classes also show
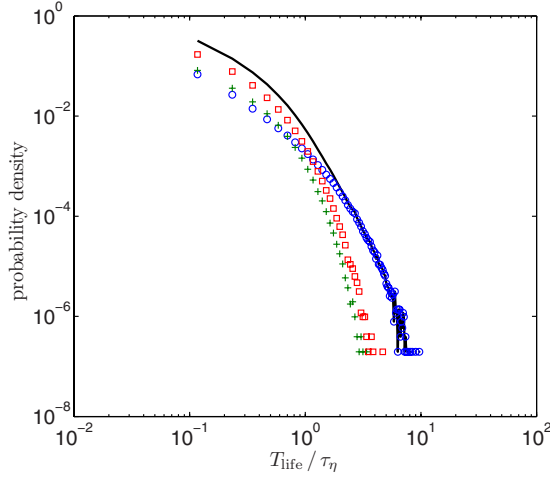
FIG. 13. (Color online) PDF and histograms of trajectory lifetimes. The solid black line is the PDF of all ZAP trajectory lifetimes. The blue ($\bigcirc$), green (+), and red ($\square$) symbols represent vortical, straining, and anti-ZAP histograms, respectively. The histograms are normalized so that the sum adds up to the PDF of all ZAPs. Note that the ratio of anti- to straining ZAP trajectory lifetimes is roughly constant throughout the graph, whereas the vortical ZAP lifetime histogram is tilted towards longer lifetimes, crossing the straining, and anti-ZAP histograms at $\sim \tau_\eta$ and $\sim 2\tau_\eta$, respectively. Almost all trajectories with a lifetime of $3\tau_\eta$ or longer are of the vortical kind. Run C3.

the same behavior in all runs. A representative plot is shown in Fig. 13. It is apparent that the majority of ZAPs have a very short lifetime less than the time scale of the smallest eddies, $\tau_\eta \equiv \eta / u_\eta \sim T_\mathcal{L} (\mathcal{L} / \eta)^{-2/3}$.

However, it is also immediately noticeable that the longest lived ZAPs are of the vortical kind, with lifetimes observed up to the length of the simulation run, e.g., $\approx 7T_\mathcal{L}$ for run C3 (Fig. 13) [40], which is extremely long.

The histograms of the straining and anti-ZAP trajectory lifetimes are qualitatively similar to each other, with the anti-ZAP trajectories being roughly twice as abundant throughout (see also caption of Table III).

While the qualitative shapes of the PDF and histograms are very similar in all runs, the ratios of the mean lifetimes of different ZAP classes are different for the filtered and unfiltered runs as detailed in Table IV. The mean lifetimes of vortical, straining and anti-ZAPs exhibit on average ratios of 100:75:80 for the low-pass filtered runs without enstrophy

TABLE IV. Ratios of mean lifetimes of ZAP classes for different runs, normalized to mean lifetime of vortical ZAPs: vortical:straining:anti-ZAP. The average ratios for the filtered runs are 100:75:80 and for the unfiltered runs A2, B3, and C4, 100:65:74.

	$N=256$	$N=512$	$N=1024$
$k_{\text{cutoff}}=64$	100:74:76	100:75:81	100:75:83
$k_{\text{cutoff}}=128$	100:63:71	100:75:79	100:75:82
$k_{\text{cutoff}}=256$		100:65:75	100:76:81
$k_{\text{cutoff}}=512$			100:66:77

cascade and 100:65:74 for the unfiltered runs which include the enstrophy cascade range and forcing scale.

Reynolds number dependence of ZAP lifetimes

As the lifetime of a ZAP depends on the likelihood of two ZAPs meeting and annihilating, an estimate of the scaling behavior of average ZAP lifetimes can be obtained from considering a ZAP pair's relative velocity and distance. The Taylor microscale of the acceleration field, λ_a, is characteristic of the average distance between ZAPs [41], and is found to scale with η, specifically $\lambda_a \approx 0.3\eta$ (see Table III for the detailed results and its caption for the definition of λ_a and η). Given λ_a and the rms relative velocity of ZAP pairs, $\hat{\xi}'$, the average lifetime might be estimated as

$$\langle T_{\text{life}} \rangle \sim \frac{\lambda_a}{\hat{\xi}'}, \tag{33}$$

under the assumption that λ_a and $\hat{\xi}'$ are statistically independent.

Let $\mathbf{x_1}$ and $\mathbf{x_2}$ be the positions of two neighboring ZAPs which are a typical distance $\approx \lambda_a < \eta$ apart from each other. The fluid velocities at both positions can be related by the approximation

$$\mathbf{u}(\mathbf{x_1}) \approx \mathbf{u}(\mathbf{x_2}) + \Delta \mathbf{x} \cdot \nabla \mathbf{u}(\mathbf{x_2}) + \mathcal{O}[\Delta x^2], \tag{34}$$

where $\Delta \mathbf{x} = \mathbf{x_1} - \mathbf{x_2}$. The relative velocity between the two ZAPs is then given by

$$\hat{\xi} = [\mathbf{V}_a(\mathbf{x_1}) - \mathbf{V}_a(\mathbf{x_2})] \cdot \frac{\Delta \mathbf{x}}{|\Delta \mathbf{x}|}$$

$$= \Delta \mathbf{x} \cdot \nabla \mathbf{u_2} \cdot \frac{\Delta \mathbf{x}}{|\Delta \mathbf{x}|} - \Delta \xi \cdot \frac{\Delta \mathbf{x}}{|\Delta \mathbf{x}|} + \mathcal{O}[\Delta x^2], \tag{35}$$

where $\mathbf{u_2} = \mathbf{u}(\mathbf{x_2})$ and $\Delta \xi = \xi(\mathbf{x_1}) - \xi(\mathbf{x_2})$. The scaling behavior of the first term is given by Kolmogorov scaling under the usual assumption of statistical independence, i.e.,

$$\left(\Delta \mathbf{x} \cdot \nabla \mathbf{u}(\mathbf{x_2}) \cdot \frac{\Delta \mathbf{x}}{|\Delta \mathbf{x}|} \right)_{\text{rms}} \sim \lambda_a \cdot \frac{u_\eta}{\eta} \sim u_\eta, \tag{36}$$

and $\Delta \xi \cdot \Delta \mathbf{x} / |\Delta \mathbf{x}|$ is also expected to scale with u_η, albeit with possible minor deviations which matter if the mix of states which is present when considering the set of all ZAPs (as discussed in Sec. V C) is relevant in the calculation of $\langle T_{\text{life}} \rangle$. Thus, in the absence of such deviations, the average ZAP lifetime $\langle T_{\text{life}} \rangle$ may be estimated to scale as $\tau_\eta = \eta / u_\eta$, i.e.,

$$\langle T_{\text{life}} \rangle \sim \tau_\eta. \tag{37}$$

The best fit exponent from scaling the average lifetimes of all ZAP trajectories, as shown in Fig. 14, is

$$\langle T_{\text{life}} \rangle \sim \tau_\eta \left(\frac{\mathcal{L}}{\eta} \right)^{-(0.093 \pm 0.016)}. \tag{38}$$

and thus is in agreement with the expectation that the average lifetime scales $\sim \tau_\eta$ with a minor correction. The scaling behavior of the different ZAP classes is identical, as indi-
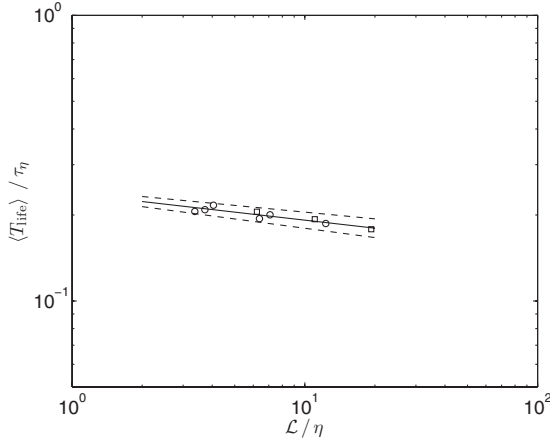
FIG. 14. Reynolds number dependence of mean ZAP trajectory lifetime. The circles (○) are data points from all (i.e., vortical, straining, and anti-) ZAP trajectories from the filtered runs and the squares (□) represent all ZAP trajectories from the unfiltered runs. The solid line is $\propto (\mathcal{L}/\eta)^{-(0.093\pm0.016)}$, the dashed lines indicate the 1σ confidence interval of the fit.

cated by the approximately constant ratio of mean ZAP lifetimes given in Table IV.

Following Sec. V C and assuming that the contribution from the $\Delta\xi$ term dominates the scaling Eq. (33), the average lifetime of ZAP trajectories is expected to scale as

$$\langle T_{\text{life}} \rangle \sim \tau_\eta \left(\frac{\mathcal{L}}{\eta} \right)^{-(0.076\pm0.008)}, \quad (39)$$

where we used $p_{\text{all}} = -(0.257\pm0.008)$ from Eq. (24) as the scaling exponent for $\hat{\xi}'$ and $u' \sim u_\eta(\mathcal{L}/\eta)^{1/3}$ to obtain the numerical value of the exponent expected from the results in Sec. V C.

While the numerical values of the exponents in Eqs. (38) and (39) agree with each other, note that this observation is only valid within the range of values of $\mathcal{L}/\eta$ presented in this paper. There are in particular two circumstances which demand further investigation if one was to attempt to extrapolate the average lifetime scalings Eqs. (38) and (39) to higher $\mathcal{L}/\eta$.

Firstly, consider the PDF of trajectory lifetimes shown for different $\mathcal{L}/\eta$ in Fig. 15. In the figure, two qualitatively different regions are indicated which could be identified with short- and long-lived trajectories. The PDF in the domain of long-lived ZAPs collapse well under the normalization $T_{\text{life}}/\tau_\eta$. However, the trendlines in Fig. 15 indicate that the slope of the PDFs increases with $\mathcal{L}/\eta$ in the domain of short-lived ZAPs, approaching the slope which is present near longer lifetimes. This change of slope causes the minor correction to the scaling exponent. It is conceivable that this slope near short lifetimes asymptotes towards the value of the slope near longer lifetimes, implying that the PDF of T_{life} fully collapses with the time scale τ_η as $\mathcal{L}/\eta \to \infty$, and therefore that the scaling of ZAP lifetimes approaches

$$\langle T_{\text{life}} \rangle \sim \tau_\eta \quad \text{as} \quad \frac{\mathcal{L}}{\eta} \to \infty. \quad (40)$$

Secondly, as discussed in Sec. III, numerical gaps might still be present in the trajectories, thus increasing the slope of the

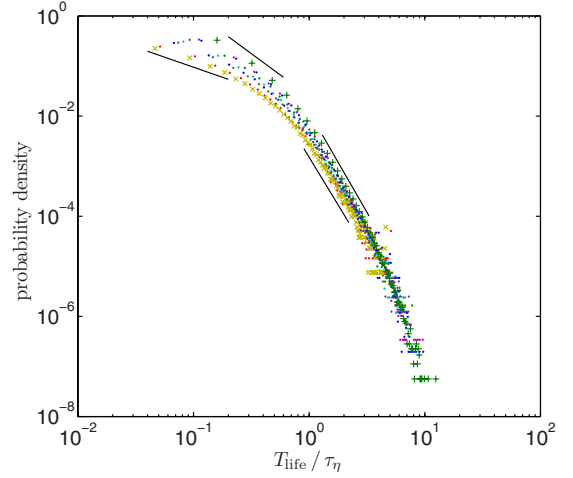FIG. 15. (Color online) PDF of trajectory lifetimes for all classes of ZAPs, for different ratios $\mathcal{L}/\eta$. The PDF with the lowest $\mathcal{L}/\eta$ is marked with the symbol ×, the PDF with the highest with +. Note that the steepness of the indicated trendlines changes sharply between the extremal ratios $\mathcal{L}/\eta$ for short-lived trajectories and hardly at all for the long-lived ones. All filtered and unfiltered runs are included.

lifetime PDF, i.e., the occurrence of a (broken) long trajectory is shifted towards short trajectories in the PDF, where it now contributes as two (or more) trajectory fragments. Hence, the algorithm employed to find the trajectories introduces its own bias, and thus is likely to influence the PDF of ZAP lifetimes (Fig. 15) and therefore also $\langle T_{\text{life}} \rangle$. In particular, this bias may itself differ with varying $\mathcal{L}/\eta$ and therefore introduce its own spurious $\mathcal{L}/\eta$ scaling in $\langle T_{\text{life}} \rangle$, hence returning Eqs. (38) and (39) instead of Eq. (40). A numerical method similar to the one described in [30] might be better suited to obtain gap-free trajectories, and thus, more confidence in the scaling of lifetime PDFs. Furthermore, trajectories at the very short end of the lifetime PDF only travel a very short distance during their existence, which can be as small as a grid cell of the interpolation grid with resolution N_a (see Sec. III), or even smaller. Thus, the detection of such short trajectories is more prone to numerical errors than that of long-lived trajectories, deteriorating the quality of the lifetime PDF at the short-lived end.

Hence, we conclude that $\langle T_{\text{life}} \rangle \sim \tau_\eta$ to a good approximation and that further work is needed to settle any small correction that there may be to this scaling. Future studies aimed at this issue will require higher $\mathcal{L}/\eta$ and a different numerical algorithm to obtain ZAP trajectories.

VII. LOCAL NEIGHBORHOOD OF ZAPS

After investigating properties of ZAPs themselves, we now turn our attention to the local flow field surrounding different classes of ZAPs.

A. Flow classification

The pitchfork diagram in Fig. 6 is very similar for all points in the flow to what it is for all ZAPs. It is therefore
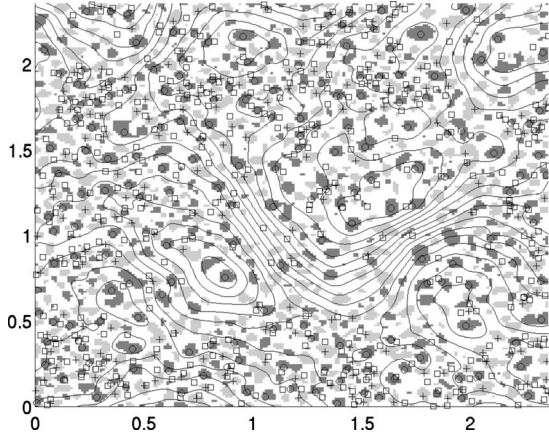
FIG. 16. ZAPs and flow regions for run A1. The size of the domain plotted is $3\pi/4 \times 3\pi/4$ which corresponds to 192×192 grid points or 5.9×5.9 integral length scales $\mathcal{L}$. Vortical ZAPs and regions are shown as circles ($\bigcirc$) and dark gray patches, straining ZAPs and regions as crosses ($+$) and light gray patches and anti-ZAPS and mediating regions as squares ($\square$) and white regions. Streamlines of the velocity field are shown as solid black lines.

tempting to apply our ZAP classification to any point in the flow. Preempting this section's conclusion, it turns out that the flow is split into regions of typical size λ_a which are either of *vortical*, *straining*, or *mediating* (term related to anti-ZAPs and explained in the next paragraph) kind.

Vortical regions are such that $\det(\nabla \mathbf{a}) > 0$ and $\nabla \cdot \mathbf{a} < 0$ whereas straining regions are such that $\det(\nabla \mathbf{a}) > 0$ and $\nabla \cdot \mathbf{a} > 0$. It is clear from Fig. 6 that the probability to find a point in the flow where $\det(\nabla \mathbf{a}) > 0$ and $\nabla \cdot \mathbf{a} = 0$ is essentially zero. Consequently, vortical and straining regions cannot be adjacent to each other; they must be separated by a mediating region, where $\det(\nabla \mathbf{a}) < 0$, hence the term "mediating."

This separation of regions is clearly seen in Fig. 16, where vortical and straining regions are surrounded by mediating regions and not directly adjacent to each other. Furthermore, this observation is consistent with Fig. 17 which shows PDFs of the distance between points in the flow and their respective nearest ZAP. The nine PDFs shown arise from the nine possible combinations of the three types of flow point and ZAP classes.

There are three distinct positions for the peaks of the PDFs in Fig. 17: the peak at the smallest distance $d < \lambda_a$ occurs when the flow point and ZAP are of the same class, which can be understood as being representative of the immediate neighborhood of a ZAP. The peak at intermediate distances $1 < d/\lambda_a < 2$ occurs when one of the flow point or ZAP is vortical or straining and the other is mediating or Anti-ZAP. Lastly, the peak at the largest distance $d > 2\lambda_a$ occurs for the two cases when flow point and ZAP are vortical and straining, thus confirming that the distance between a flow point in a vortical region and a ZAP in a straining region must be on average larger than in the other cases because vortical and straining regions cannot be adjacent.

B. Local flow patterns around ZAPs

The degenerate nature of the eigenvalues of $\nabla \mathbf{a}$ at vortical and straining ZAPs implies, as explained in Sec. IV B, that
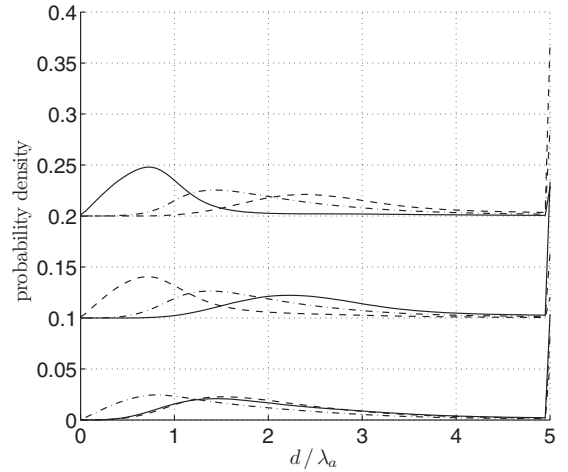

FIG. 17. PDF of distance between arbitrary points in the flow and nearest ZAP. Shown are vortical (solid line), straining (dashed line), and mediating (dash-dotted line) points in the flow, grouped together (by shifting along the vertical axis) according to the class of the nearest neighbor ZAP (vortical, straining and anti-ZAP, top to bottom). Run C3.

the acceleration at a point near to such a ZAP is aligned with the distance vector of that point to the ZAP.

We thus expect that the acceleration vector $\mathbf{a}$ at a point $\mathbf{x}$ in the flow near enough a vortical ZAP at $\mathbf{x_a}$ to be approximately parallel to the vector $\mathbf{n} \equiv \mathbf{x_a} - \mathbf{x}$. Furthermore, for a straining ZAP, we expect these vectors to be approximately antiparallel. However, no such alignment is expected in the close neighborhood of an anti-ZAP (see Sec. IV B).

Figure 18 confirms these expected alignments for vortical and straining ZAPs while no predominant alignment is visible for anti-ZAPs. Note that the alignment is best at flow points close to the ZAP, i.e., from the same kind of region as
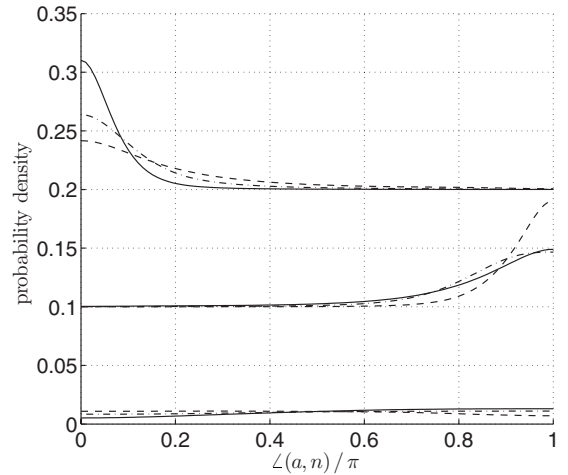

FIG. 18. PDF of angles between the acceleration vector, $\mathbf{a}$, and the vector connecting arbitrary points in the flow with their respective nearest ZAP, $\mathbf{n}$. Shown are vortical (solid line), straining (dashed line) and mediating (dash-dotted line) points in the flow, grouped together (by shifting along the vertical axis) according to the class of the nearest neighbor ZAP (vortical, straining, and anti-ZAP, top to bottom). Run C3.
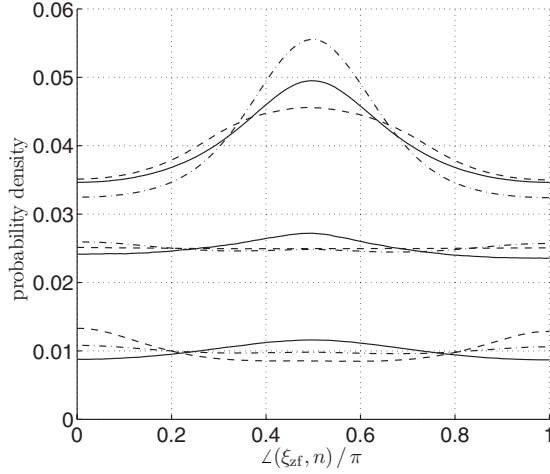
FIG. 19. PDF of angles between the velocity vector in the nearest ZAP frame, ξ_{zf}, and the vector connecting arbitrary points in the flow with their respective nearest ZAP, **n**. Shown are vortical (solid line), straining (dashed line), and mediating (dash-dotted line) points in the flow, grouped together (by shifting along the vertical axis) according to the class of the nearest neighbor ZAP (vortical, straining, and anti-ZAP, top to bottom). Run C3.

the ZAP, but it is still significant at flow points further away as indicated by the PDFs for the cases where the type of the region containing the flow point is different from the ZAP class. Moreover, when conditioning these PDFs on the distance d between flow point and ZAP, the shape of the PDF remains approximately the same for $0 \lesssim d \lesssim 5\lambda_a$ and even beyond.

The degenerate nature of the eigenvalues of $\nabla\mathbf{a}$ at, and the good sweeping properties of, vortical ZAPs suggest that the local flow velocity at points close to the nearest ZAP is approximately perpendicular to the acceleration vector **a** and thus also to the vector $\mathbf{n} = \mathbf{x_a} - \mathbf{x}$, if the ZAP is vortical and if this flow velocity ξ_{zf} is measured in the frame moving with that ZAP, i.e.,

$$\xi_{zf}(\mathbf{x}) \equiv \mathbf{u}(\mathbf{x}) - \mathbf{V_a}(\mathbf{x_a}) \perp \mathbf{n}, \tag{41}$$

where $\mathbf{x_a}$ is the position of the ZAP nearest to **x**. The implication behind the sweeping property is that the flow velocity at **x** is effectively frozen in the frame moving with $\mathbf{V_a}(\mathbf{x_a})$.

As illustrated by Fig. 19, this prediction is approximately satisfied, thus demonstrating how powerful $\mathbf{V_a}$ can be in taking into account the time dependence of local flow patterns in some cases. Note that the sharpest peak around $\angle(\xi_{zf}, \mathbf{n}) = \pi/2$ for vortical ZAPs is for mediating flow points. This behavior is likely due to the prevailing deviations from $\xi_{zf}(\mathbf{x_a}) = 0$ (see Sec. V), thus spoiling the alignment of ξ_{zf} and **n** at very small distances $d = |\mathbf{n}|$, i.e., in the very near neighborhood where the flow region is also of the vortical kind. As for the alignment of **a** and **n**, the shapes of these PDFs for vortical ZAPs (Fig. 19, top) remain approximately similar for $0 \lesssim d \lesssim 5\lambda_a$ and beyond. The PDFs for other ZAPs seem to show some weak preferred alignments, but they are not very clear and we leave them for future study.

C. Estimating the size of vortical flow structures

As we have shown, the influence of a ZAP on the flow field stretches at least as far as $5\lambda_a$ in run C3. We now try to estimate how large the observed flow patterns and associated coherent structures surrounding ZAPs can be. In Sec. VII B, we found a noticeable signature of coherent eddies surrounding vortical ZAPs in the observable flow velocity and acceleration fields. Thus, we now attempt to find this signature in a larger neighborhood of vortical ZAPs.

Since the expected size of the structures is larger than the average distance between ZAPs, using the nearest ZAP as a point of reference for the local velocity frame is not recommended as the nearest ZAP might not be the one defining the effectively frozen flow pattern at the point **x** in the region under investigation.

Instead, we make the assumption that the velocity of the reference frame in which the coherent eddy appears to be approximately frozen (see Sec. VII B) varies only by a negligible amount throughout the frozen flow pattern,

$$\mathbf{V_a}(\mathbf{x}) \approx \mathbf{V_a}(\mathbf{x_{a,ref}}), \tag{42}$$

where $\mathbf{V_a}(\mathbf{x_{a,ref}})$ is the velocity of the ZAP that defines the reference frame and $\mathbf{V_a}(\mathbf{x})$ is the *constant acceleration point* (CAP) velocity of a point belonging to the flow structure.

Note that the CAP velocity $\mathbf{V_a}(\mathbf{x})$ is defined by Eq. (2) in the same way as for ZAPs, but for any point in the flow, i.e., also where $|\mathbf{a}| \neq 0$. A CAP follows the trajectory of an acceleration vector which is constant in magnitude and direction, and thus its existence is more sensitive to fluctuations in the acceleration field than a ZAP. In particular, we expect points with $\det(\nabla\mathbf{a}) = 0$ to occur in areas of size λ_a, and hence, a frozen flow pattern, which we have seen to extend to several λ_a in size, is very likely to have points where $\det(\nabla\mathbf{a}) = 0$, and thus $\mathbf{V_a} \rightarrow \infty$. However, the majority of CAPs have nonsingular velocities and thus, we assume that Eq. (42) is a suitable approximation when considering statistics of entire flow patterns.

The local fluid velocity in the CAP frame of reference can also be defined as

$$\xi(\mathbf{x}) \equiv \mathbf{u}(\mathbf{x}) - \mathbf{V_a}(\mathbf{x}), \tag{43}$$

similar to Eq. (41), but for CAPs as well as for ZAPs. It was first pointed out by Schwander *et al.* [34] that the PDF of ξ_1 transverse to the acceleration component a_2 is bimodal for accelerations $|\mathbf{a}| \gtrsim a'$, likely due to the presence of intense vortices in the isotropic turbulent flow. We now confirm this finding (Fig. 20) and use it to estimate the size of vortical flow structures.

Assuming circular flow patterns in the reference frames of coherent eddies, we expect

$$\xi(\mathbf{x}) = \mathbf{u}(\mathbf{x}) - \mathbf{V_a}(\mathbf{x}) \perp \mathbf{a}(\mathbf{x}) \tag{44}$$

to be approximately satisfied for regions in which vortical flow structures exist. Thus, the relation between the perpendicular components ξ_1 and a_2 for circular motion, i.e.,
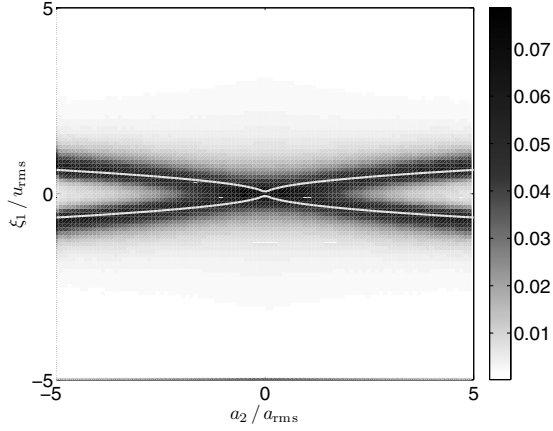
FIG. 20. Conditional PDF of ξ_1 along vertical axis, conditioned on a_2 (horizontal axis). Data from vortical flow regions of run C3. Grey lines indicate expected velocity profiles $\xi_1 = \pm\sqrt{r_{\mathrm{circ}}|a_2|}$ from circular motion with highest probability averaged along the shown lines. In this case $r_{\mathrm{curv}} \approx 11\lambda_a$. This plot is qualitatively the same for vortical, mediating, and all regions combined in all runs, but not for straining regions.

$$|a_2| = \frac{\xi_1^2}{r_{\mathrm{curv}}} \Rightarrow \xi_1 = \pm\sqrt{r_{\mathrm{curv}}|a_2|}, \qquad (45)$$

can be used for an approximate determination of a curvature radius, r_{curv}. This can be done by tracing how the peak of the a_2-conditioned PDF of ξ_1 depends on a_2. Figure 20 is a plot of this conditional PDF as well as of Eq. (45) and is representative of the similar plots for vortical, mediating and all combined regions of all runs. (This last case is the one studied in [34].) However, this plot is very different for straining regions, where circular structures are not to be expected, and where Eqs. (44) and (45) cannot hold.

The most probable r_{curv} from all runs and suitable kinds of regions are shown in Fig. 21. First of all, note how r_{curv} is much larger than $\lambda_a \approx 0.3\eta$ in all cases (e.g. $r_{\mathrm{curv}} \approx 11\lambda_a$ in run C3, see caption of Fig. 20) and thus considerably larger than the average distance between ZAPs. Secondly, the observed scaling exponent indicates that the size of the vortical flow patterns does not scale with the average distance between ZAPs, $r_{\mathrm{curv}} \not\propto \lambda_a \sim \eta$, but with a length-scale between η and $\mathcal{L}$.

The Taylor microscale $\lambda \sim \eta(\mathcal{L}/\eta)^{1/3}$ is the expected length-scale which characterizes the size of flow structures in the velocity field [16,36]. However, the scaling exponent found in Fig. 21 is steeper than 1/3. Given the uncertainty arising from the approximations made in obtaining r_{curv}, we feel that it is not viable to conclude whether the observed scaling is in agreement with λ or not.

We do conclude, however, that structures centered around ZAPs can be significantly larger than the distance between ZAPs. The characteristic size of these vortical structures is found to scale with a length-scale larger than η, and thus also larger than λ_a.

VIII. SUMMARY OF CONCLUSIONS

We now draw all our observations together into a consistent picture of ZAPs in two-dimensional stationary homogeneous isotropic turbulence.
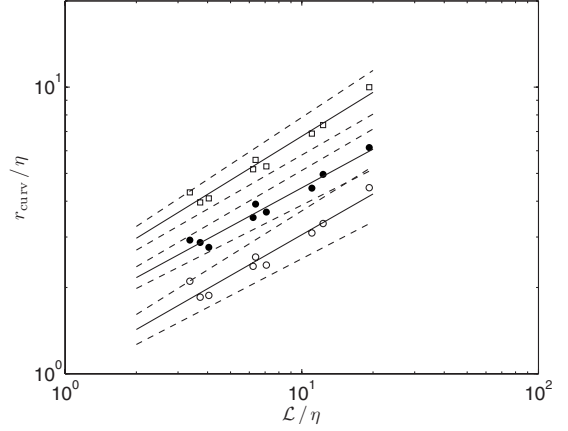

FIG. 21. Reynolds number dependence of most probable r_{curv} of vortical flow patterns across all runs. The bullets ($\bullet$), circles ($\circ$), and squares ($\square$) are data points from all, vortical and mediating regions, respectively. The solid line indicates a fit of $r_{\mathrm{curv}}/\eta \propto (\mathcal{L}/\eta)^p$, the dashed lines indicate the 1σ confidence intervals of the fits. The best fit exponents found are $p(\bullet) = (0.448 \pm 0.033)$, $p(\circ) = (0.473 \pm 0.045)$, and $p(\square) = (0.509 \pm 0.036)$. Note that the quoted confidence intervals represent only the scatter of the individual data points, not the uncertainty in obtaining the data points. The total confidence interval, combining all uncertainties, is likely to be a multiple of the quote one (see text).

ZAPs are not pressure extrema. They are points where a nonzero pressure gradient balances a nonzero dissipative force. The range of values taken by this dissipative force at ZAPs is indicative of the range of its values over the entire flow.

The antisymmetric part of the tensor $\nabla\mathbf{a}$ is generally negligible compared to the symmetric part (Fig. 4). Furthermore, the distribution of ZAPs in the space spanned by the two invariants of the acceleration gradient tensor, $\nabla\cdot\mathbf{a}$ and $\det(\nabla\mathbf{a})$, exhibits three distinct branches in all simulation runs (Fig. 6). This pitchfork structure with three distinct branches is not limited to ZAPs, but also holds when all flow points are sampled.

The three branches suggest a classification of three ZAP types: vortical and straining ZAPs, both with a positive determinant of $\nabla\mathbf{a}$, and anti-ZAPs with a negative determinant. Topological constraints on the acceleration field imply that ZAPs are created and destroyed in pairs, where a pair always consists of a ZAP with positive determinant and an anti-ZAP. As a result, 50% of all ZAPs are anti-ZAPs. The number of vortical and straining ZAPs is about the same.

Note that vortical and straining *velocity stagnation points* (VSPs) annihilate pairwise directly without the need for a mediating "anti-VSP" (which, in fact, does not exist). The vortical VSPs have a positive determinant of $\nabla\mathbf{u}$ and the straining ones a negative determinant, and thus, by virtue of the usual bifurcations of vector fields referred to in Sec. II B, these two kinds of critical points of the velocity field can annihilate directly.

Aside from the ZAP class, which is fixed throughout the lifetime of a ZAP, a ZAP can be in different states which change during its lifetime. Near creation or destruction, where $|\mathbf{V_a}| \to \infty$, ZAPs are in a near-singular state where no

sweeping can be observed. When ZAPs are not in this state, vortical and straining ZAPs are typically swept by the local fluid velocity, a state which is characterized by $|\xi| \ll u'$.

Vortical and straining ZAPs are different in their sweeping behavior compared to anti-ZAPs. While the former are generally swept by the local fluid velocity to an acceptable statistical approximation, we find no clear evidence that anti-ZAPs are swept. Instead, a positive correlation between ξ and **u** exists for Anti-ZAPs. Long-lived vortical and straining ZAPs are on average swept, and short-lived ZAPs of these kinds are dominated by the creation and destruction events where the ZAP velocity $|\mathbf{V_a}| \rightarrow \infty$. Long-lived ZAP trajectories show a better sweeping behavior with increasing Reynolds number, thus underpinning Tennekes' sweeping hypothesis [24,34,35].

Vortical ZAPs are on average the longest lived, straining ones on average the shortest. However, irrespective of ZAP class, the vast majority of ZAPs are short-lived with lifetimes smaller than the time scale of the smallest eddies, and therefore in a near-singular state. Nevertheless, the average ZAP lifetime seems to scale with that time scale. The longest lived ZAPs are of vortical kind, suggesting that the associated flow configuration is the most stable, capable of surviving for times as long as a few integral time scales.

Hence, out of the many ZAPs in a flow, only a small number lives sufficiently long to be associated with persistent coherent structures. It is these few points that have the potential to characterize the mixing and transport properties of a flow through their relation to coherent structures. The short-lived majority of ZAPs is unlikely to influence coherent structures, but can still have an important physical significance in other areas such as clustering of inertial particles. Indeed, the clear spatial correlation which exists between clusters of inertial particles and clusters of ZAPs and which has recently been reported in [24–26] is not in disagreement with short-lived ZAPs. The relevant time scale for this clustering correlation is that of the ZAP cluster, less so that of the ZAPs themselves which in fact live long enough within the cluster for the sweep-stik mechanism to take hold and for particles to bounce from ZAP to ZAP within the cluster [24–26]. It is important to note that the higher density of ZAPs in a cluster implies a higher probability of collisions and thus destructions, and hence, it should come as no surprise that ZAPs in a dense cluster have a shorter lifetime than their more isolated peers.

The application of the proposed classification to the entire flow shows that vortical and straining regions cannot be adjacent and thus, are always separated by a mediating flow region, which contains anti-ZAPs.

Moreover, structures around vortical ZAPs can be significantly larger than λ_a. Hence, it is possible that several ZAPs occur within the area belonging to one structure, with one ZAP near the center dominating the whole structure. An al-

ternative (or additional) explanation might be that there are big voids around dominant vortical ZAPs, which contain no ZAPs at all. Voids like these have been observed in a study of clustering of inertial particles [24].

The size of these structures typically scales with a length scale larger than the characteristic distance λ_a between ZAPs, and $\lambda_a \sim \eta$. There is not enough evidence in the current data analysis to link this size to the Taylor microscale λ of the *velocity* field, but a relation between the size of these structures and λ can also not be excluded.

APPENDIX: GAP FINDING METHOD

To identify potential gaps in the numerically determined trajectories of ZAPs, we first examine all beginnings and endings of trajectories. As discussed in Sec. II B, ZAPs are necessarily created and destroyed in pairs. Thus, we shall use the presence of a suitable creation or destruction partner ZAP as an indicator for a trajectory having an orderly beginning or end. If a suitable partner ZAP cannot be located, we assume that the trajectory-beginning or -ending is due to numerical issues and thus, bordering a gap.

We further assume a suitable partner ZAP to be present if it is within a temporal threshold of one time step and a spatial threshold of $2\mathrm{d}x = \pi/N$ (i.e. two grid points' distance). If no matching partner ZAP for a trajectory's ending can be found, we carry out a search for a suitable partnerless trajectory-beginning within a cone in space time originating at the position of the trajectory-ending bordering a gap, $\mathbf{x}_{\mathrm{end}}$. That is, the 25 following time steps are examined to look for a suitable trajectory-beginning within a circle of radius $i\mathrm{d}x/2$ around the position $\mathbf{x}_{\mathrm{end}} + i\mathbf{V_a}(\mathbf{x}_{\mathrm{end}})\mathrm{d}t$, where i is enumerating the number of time steps into the future. I.e., the expected position of the missing ZAPs is extrapolated from $\mathbf{V_a}(\mathbf{x}_{\mathrm{end}})$ and the search radius increases linearly with the temporal distance from the trajectory-ending which is bordering the gap.

If one or more suitable trajectory-beginnings are found within the search cone, the closest in time (and then in space) is taken to be the match for the trajectory-ending at which the search originated. The thus identified gap is closed by linearly interpolating all recorded quantities [$\mathbf{x_a}$, $\mathbf{V_a}$, ξ, $\det(\nabla \mathbf{a})$ and $\nabla \cdot \mathbf{a}$] and fusing the trajectory fragments. This search is carried out for all trajectory-endings which are suspected to border a gap at all time steps, excluding the first and last time step.

[1] Garry L. Brown and Anatol Roshko, J. Fluid Mech. **64**, 775 (1974).

[2] B. Fornberg, J. Comput. Phys. **25**, 1 (1977).

[3] Wm. T. Ashurst, A. R. Kerstein, R. M. Kerr, and C. H. Gibson, Phys. Fluids **30**, 2343 (1987).

[4] Paul M. Bevilaqua and Paul S. Lykoudis, J. Fluid Mech. **89**, 589 (1978).

[5] C. Basdevant, B. Legras, R. Sadourny, and M. B'eland, J. Atmos. Sci. **38**, 2305 (1981).

[6] Eric D. Siggia, J. Fluid Mech. **107**, 375 (1981).

[7] James C. McWilliams, J. Fluid Mech. **146**, 21 (1984).

[8] A. A. Wray and J. C. R. Hunt, *Topological Fluid Mechanics: Proceedings of the IUTAM Symposium* (Cambridge University Press, Cambridge, UK, 1990), pp. 95–104.

[9] J. Weiss, Physica D **48**, 273 (1991).

[10] A. Provenzale, Annu. Rev. Fluid Mech. **31**, 55 (1999).

[11] A. Bracco, J. von Hardenberg, A. Provenzale, J. B. Weiss, and J. C. McWilliams, Phys. Rev. Lett. **92**, 084501 (2004).

[12] G. Haller and G. Yuan, Physica D **147**, 352 (2000).

[13] N. Peters and L. Wang, Compt. Rend. **334**, 493 (2006). Observation, analysis and modeling in complex fluid media- Special issue for the 60th birthday of Professor Roland Borghi.

[14] J. C. H. Fung and J. C. Vassilicos, Phys. Rev. E **57**, 1677 (1998).

[15] J. Dávila and J. C. Vassilicos, Phys. Rev. Lett. **91**, 144501 (2003).

[16] Susumu Goto and J. C. Vassilicos, New J. Phys. **6**, 65 (2004).

[17] T. Faber and J. C. Vassilicos, Phys. Fluids **21**, 015106 (2009).

[18] A. E. Perry and B. D. Fairlie, Adv. Geophys. **18**, 299 (1975).

[19] A. E. Perry and M. S. Chong, Annu. Rev. Fluid Mech. **19**, 125 (1987).

[20] A. E. Perry and M. S. Chong, Appl. Sci. Res. **53**, 357 (1994).

[21] Nicholas T. Ouellette and J. P. Gollub, Phys. Rev. Lett. **99**, 194502 (2007).

[22] S. Goto, D. R. Osborne, J. C. Vassilicos, and J. D. Haigh, Phys. Rev. E **71**, 015301 (2005).

[23] Raymond A. Shaw, Annu. Rev. Fluid Mech. **35**, 183 (2003).

[24] L. Chen, S. Goto, and J. C. Vassilicos, J. Fluid Mech. **553**, 143 (2006).

[25] Susumu Goto and J. C. Vassilicos, Phys. Fluids **18**, 115103 (2006).

[26] S. W. Coleman and J. C. Vassilicos, Phys. Fluids **21**, 113301 (2009).

[27] B. L. Hua and P. Klein, Physica D **113**, 98 (1998).

[28] A. Okubo, Deep-Sea Res. Oceanogr. Abstr. **17**, 445 (1970).

[29] John Guckenheimer and Philip Holmes, *Nonlinear Oscillations, Dynamical Systems, and Bifurcations of Vector Fields*, Applied Mathematical Sciences Vol. 42, 7th ed. (Springer, New York, 2002).

[30] X. Tricoche, T. Wischgoll, G. Scheuermann, and H. Hagen, Comput. Graph. **26**, 249 (2002).

[31] P. Schmelcher and F. K. Diakonos, Phys. Rev. Lett. **78**, 4733 (1997).

[32] Prakash Vedula and P. K. Yeung, Phys. Fluids **11**, 1208 (1999).

[33] A. Tsinober, P. Vedula, and P. K. Yeung, Phys. Fluids **13**, 1974 (2001).

[34] F. Schwander, E. Hascoet, and J. C. Vassilicos, Phys. Rev. E **79**, 015301 (2009).

[35] H. Tennekes, J. Fluid Mech. **67**, 561 (1975).

[36] Susumu Goto and J. C. Vassilicos, Phys. Fluids **21**, 035104 (2009).

[37] Note that the vorticity field is only low-pass filtered for the purpose of calculating the velocity, acceleration, and other quantities. The DNS time integration is carried out using the unfiltered vorticity field.

[38] For convenience of notation, we defined that the density $\rho = 1$.

[39] The argument goes as follows: $\xi = 0$ implies $\partial \mathbf{a}/\partial t + \mathbf{u} \cdot \nabla \mathbf{a} = \xi \cdot \nabla \mathbf{a} = 0$, hence the acceleration of a fluid element is constant and only $\mathbf{a} = 0$ can be a solution for a prolonged time due to the limited kinetic energy of a fluid element. Thus, the velocity of the fluid element, and hence the ZAP, is its initial one.

[40] The length of the individual simulation runs was chosen so that the lifetime PDF is well resolved, i.e., the number of trajectories with a lifetime equal or greater than the simulation length should be of the same order as the number of trajectories contributing to the longest lifetime data point in the PDF.

[41] The proof of the generalized Rice theorem given in [36] can also be applied to the acceleration field of this paper's turbulent flow. The Taylor microscale of acceleration, λ_a, is therefore proportional to the average distance between ZAPs. Furthermore, since the fractal dimension of the set of ZAPs is 2 in energy-cascading two-dimensional turbulence, as shown in [16], the average length between ZAPs is also the characteristic length between ZAPs. For these reasons, Eq. (33) is a good estimate of the average ZAP lifetime.